Undrained cylindrical cavity expansion in clays with fabric anisotropy and structure: theoretical solution

by

Nallathamby Sivasithamparam (1) and Jorge Castro (2)(*)

E-mail: (1) nallathamby.siva@ngi.no ; (2) castrogj@unican.es

Affiliation:

(1) PhD, Senior engineer, Computational Geomechanics Division, Norwegian Geotechnical Institute, Oslo, Norway

(2) PhD, Senior lecturer, Department of Ground Engineering and Materials Science, University of Cantabria, Santander, Spain

(*) Corresponding author:

Group of Geotechnical Engineering
Department of Ground Engineering and Materials Science
University of Cantabria
Avda. de Los Castros, s/n
39005 Santander, Spain
Tel.: +34 942 201813
Fax: +34 942 201821
e-mail: castrogj@unican.es

Date: November 2019

Number of words: 6,000

Number of tables: 4

Number of figures: 16

Abstract

This paper presents a novel, exact, semi-analytical solution for the quasi-static undrained expansion of a cylindrical cavity in soft soils with fabric anisotropy and structure. The assumed constitutive model is the S-CLAY1S model, which is a Cam clay type model that considers fabric anisotropy that evolves with plastic strains, structure and gradual degradation of bonding (destructuration) due to plastic straining. The solution involves the numerical integration of a system of seven first-order ordinary differential equations, three of them corresponding to the effective stresses in cylindrical coordinates, other three corresponding to the components of the fabric tensor and one corresponding to the amount of bonding. The solution is validated against finite element analyses and analytical limit asymptotic values of the effective stresses at the cavity wall are established. When destructuration is considered, the solution provides lower values of the effective radial stresses near the cavity wall, which are partially compensated by larger values of the excess pore pressures. Parametric analyses and discussion of the influence of soil overconsolidation, initial amount of bonding and rate of destructuration are presented. Finally, the theoretical solution is compared with experimental data of undrained shear strength variation immediately after pile driving in a sensitive clay.

Keywords: Destructuration; bonding; fabric of soils; clays; cavity expansion; theoretical analysis.

1. Introduction

The theory of cavity expansion has been widely applied in geomechanical and geotechnical problems such as pressuremeter tests (e.g., Gibson and Anderson 1961; Palmer 1972), pile and stone column installation (e.g., Randolph et al. 1979; Castro and Karstunen 2010), cone penetration tests (e.g., Vesic 1972) and bearing capacity of deep foundations (e.g., Coop and Wroth 1989). Over the past decades, development of analytical or semi-analytical solutions for clays under undrained condition had mainly been focused on reconstituted (isotropic) samples (e.g., Yu 2000), ignoring the natural clay behaviour such as anisotropy and structure. More recently, semi-analytical solutions for clays using anisotropic critical state plasticity models have been presented and it is a subject undergoing intense study (Li et al. 2016; Li et al. 2017; Sivasithamparam and Castro 2018; Chen and Liu 2019; Chen et al. 2019; Li et al. in press; Liu and Chen in press, Chen et al. in press). On the other hand, solutions for cavity expansion in isotropic strain-softening soils using a post-failure strain softening (e.g., Prévost and Hoëg 1975) and interpretation of pressuremeter tests in sensitive soils (e.g., Ladd et al. 1980; Silvestri 2003; Silvestri and Tabib 2018) have been presented. However, to the best of the author's knowledge, an exact analytical or semi-analytical solution for anisotropic, structure (inter-particle bonding) and destructuration behaviour of plastic nature of clays is not yet available in the literature. Neglecting soil structure leads to inaccurate predictions of clay responses under external loading (e.g., Rouainia and Muir Wood 2000; Callisto and Rampello 2004; González et al. 2009; Deotti et al. 2017).

This paper presents a novel, exact and semi-analytical cylindrical cavity expansion solution for natural clays, which exhibit fabric anisotropy and structure. The solution is developed using the S-CLAY1S constitutive model (Karstunen et al. 2005), which considers fabric anisotropy that evolves with plastic strains, structure and gradual degradation of bonding (destructuration) due to plastic straining. In this way, this paper extends the previous work by the authors (Sivasithamparam and Castro 2018), which considered only anisotropy through the S-CLAY1 model (Wheeler et al. 2003) and was based on the semi-analytical approach for cylindrical cavity expansion problems in isotropic soils proposed by Chen and Abouisleiman (2012).

The assumptions and mathematical derivation of the semi-analytical solution are presented in Section 2. A system of seven first-order ordinary differential equations that require numerical integration is obtained. Details of the mathematical formulation are included as separate appendixes for simplicity and clarity. Validation of the semi-analytical solution against finite element analyses, results and parametric analyses are portrayed in Section 3. The solution shows that the effective radial stress at the cavity wall increases as the cavity is expanded, but it reaches a peak value and progressively decreases down to a limit asymptotic value because of the loss of bonding in the soil. Comparison with analytical limit values and discussion of the influence of soil overconsolidation, initial amount of bonding and rate of destructuration are presented. Finally, the theoretical solution is compared with experimental data of in situ vane strength variation immediately after pile driving in a sensitive clay (Section 4) and the main conclusions are summarized in Section 5.

2. Mathematical formulation and semi-analytical solution

2.1. Assumptions and basic equations

The following assumptions are made to study the quasi-static expansion of a cylindrical cavity of initial radius a_0 under undrained conditions:

1. The axis of the cylindrical cavity is assumed as the vertical axis and the initial stress state is homogeneous and consists of a horizontal effective stress and a vertical effective stress (σ'_H, σ'_V).
2. The initial stress state may be also formulated in terms of total stresses considering the initial uniform pore water pressure (u_0, σ_H, σ_V).
3. The initial horizontal stress on the cavity is also σ_H and it increases up to σ_a, upon expanding the cavity to a final radius a (Figure 1).
4. The symmetry axis of the initial soil cross-anisotropy (transversely isotropic material) is the vertical one.
5. The problem has axial symmetry, thus, shear stresses vanish and, due to the infinite extent of the soil, plane strain conditions hold.
6. Cylindrical coordinates (r,θ,z) are used throughout the paper because they are principal directions for this problem. Principal effective stresses are radial σ'_r, tangential σ'_θ and vertical σ'_z.
7. Large-strain deformation is considered in the plastic region using natural (or logarithmic) strains, but small-strain deformation is used in the elastic region.

The equilibrium equation in the radial direction for cylindrical coordinates that are principal directions using effective stresses may be written as

$$\frac{\partial \sigma'_r}{\partial r} + \frac{\partial u}{\partial r} + \frac{\sigma'_r - \sigma'_\theta}{r} = 0 \qquad (1)$$

Under undrained conditions, the current position of an arbitrary point, r_x, is directly related to the initial position of the point, r_{x0}, and the initial and current radii of the cavity, a_0 and a, yielding the following equation in dimensionless form as

$$\left(\frac{r_{x0}}{a}\right)^2=\left(\frac{r_x}{a}\right)^2+\left(\frac{a_0}{a}\right)^2-1 \qquad (2)$$

2.2. Constitutive model: S-CLAY1S

The S-CLAY1S model, developed by Karstunen et al. (2005), is an extension of the S-CLAY1 model (Wheeler et al. 2003) incorporating the influence of bonding and destructuration. In the model, anisotropic plastic behaviour is presented through an inclined yield surface and a rotational component of hardening to represent the development or erasure of fabric anisotropy during plastic straining. The effect of soil structure is introduced using intrinsic and natural yield surfaces (Gens and Nova 1993).

For the simplified conditions of a triaxial stress space and for an initial cross-anisotropy fabric with the main axis being the vertical one (e.g. a vertically cut sample), the yield function can be expressed as (Wheeler et al. 2003)

$$f_y=(q-\alpha p')^2-(M^2-\alpha^2)(p'_m-p')p \qquad (3)$$

where q is the deviatoric stress, p' is the mean effective stress, M is the critical state value of the stress ratio (where $\eta=q/p'$) and p'_m and α define the size and inclination of the natural yield curve, respectively (Figure 2).

The intrinsic yield surface is of smaller size but same orientation as the yield curve of the natural soil (Figure 2). The size of the intrinsic yield surface is defied by the state variable p'_{mi} which is linked to the size of the natural yield surface by

$$p'_m=(1+\chi)p'_{mi} \qquad (4)$$

where χ defines the amount of bonding.

S-CLAY1S incorporates three hardening laws. The first describes the change of size of the yield curve, which is assumed to be related solely to plastic volumetric strains (as in MCC)

$$dp'_{mi} = \frac{\upsilon p'_{mi}}{\lambda_i - \kappa} d\varepsilon_v^p \tag{5}$$

where υ is the specific volume, λ_i is the slope of the intrinsic post-yield compression curve in the υ-lnp' plane and κ is the slope of the swelling line in the compression plane.

The second hardening law (rotational hardening) describes the change of inclination of the yield curve produced by plastic straining, both volumetric and shear strains.

$$d\alpha = \omega \left[\left(\frac{3\eta}{4} - \alpha \right) \langle d\varepsilon_v^p \rangle + \omega_d \left(\frac{\eta}{3} - \alpha \right) \left| d\varepsilon_d^p \right| \right] \tag{6}$$

where ω is a material constant that controls the absolute effectiveness of plastic strains in rotating the yield surface towards the target value. Similarly, ω_d controls the relative effectiveness of shear and volumetric strains.

The third destructuration law (Karstunen et al. 2005) describes the degradation of bonding with plastic straining by both volumetric and shear strains.

$$d\chi = -\xi \chi \left(\left| d\varepsilon_v^p \right| + \xi_d \left| d\varepsilon_d^p \right| \right) \tag{7}$$

where ξ and ξ_d are two additional model constants controlling the rate of degradation (in an analogous manner to ω and ω_d in Eq. 6). Full details of the hardening laws and determination of the model constants may be found in (Wheeler et al. 2003; Karstunen et al. 2005).

2.3. Invariants

The natural yield surface of the model (Figure 2) can be expressed in generalized form as

$$f_y = \frac{3}{2}(\boldsymbol{\sigma}'_{\boldsymbol{d}} - \boldsymbol{\alpha}_d p')^T(\boldsymbol{\sigma}'_{\boldsymbol{d}} - \boldsymbol{\alpha}_d p') - (M^2 - \boldsymbol{\alpha}_d^T \boldsymbol{\alpha}_d)(p'_m - p')p' \tag{8}$$

where

$$\boldsymbol{\sigma}'_{\boldsymbol{d}} = [\sigma'_r - p' \quad \sigma'_\theta - p' \quad \sigma'_z - p']^T \tag{9}$$

and

$$\boldsymbol{\alpha}_{\boldsymbol{d}} = [\alpha_r - 1 \quad \alpha_\theta - 1 \quad \alpha_z - 1]^T \tag{10}$$

$$p' = \frac{(\sigma'_r + \sigma'_\theta + \sigma'_z)}{3} \tag{11}$$

Sivasithamparam and Castro (2018) proposed a new invariant for the S-CLAY1 model ($\bar{q}$), which simplifies the development of mathematical solutions for cylindrical cavity expansion in plastic anisotropic soils. The same invariant is also adopted for S-CLAY1S

$$\bar{q} = \sqrt{\frac{3}{2}Q} \tag{12}$$

where

$$Q = (\boldsymbol{\sigma}'_{\boldsymbol{d}} - \boldsymbol{\alpha}_d p')^T(\boldsymbol{\sigma}'_{\boldsymbol{d}} - \boldsymbol{\alpha}_d p') = s_r^2 + s_\theta^2 + s_z^2 \tag{13}$$

and s_i are the following deviatoric stresses

$$s_i = \sigma_i'^d - \alpha_i^d p' = \sigma'_i - (\alpha_i^d + 1)p' \qquad \text{for } i=r,\theta,z \tag{14}$$

and α_i^d are deviatoric components of the fabric tensor.

Using this invariant ($\bar{q}$), the natural yield surface of the S-CLAY1S model can be expressed in a similar form as isotropic Cam-clay models

$$f_y = \bar{q}^2 - (M^2 - \alpha^2)(p'_m - p')p' \tag{15}$$

2.4. Elastoplastic stiffness matrix

The increments of elastic strains in r, θ and z directions may be obtained using the isotropic linear elastic stress-strain relationship as

$$\begin{Bmatrix} d\varepsilon_r^e \\ d\varepsilon_\theta^e \\ d\varepsilon_z^e \end{Bmatrix} = \frac{1}{E}\begin{bmatrix} 1 & -\nu & -\nu \\ -\nu & 1 & -\nu \\ -\nu & -\nu & 1 \end{bmatrix} \cdot \begin{Bmatrix} d\sigma_r' \\ d\sigma_\theta' \\ d\sigma_z' \end{Bmatrix} \tag{16}$$

where Young's modulus E is defined in terms of shear modulus G and Poisson's ratio ν as $E = G(1+\nu)$. (17)

G is calculated in the S-CLAY1S model using the current stress state as

$$G = \frac{3(1-2\nu)\upsilon}{2(1+\nu)\kappa} p' \tag{18}$$

The components of plastic strain increments $d\boldsymbol{\varepsilon}^p$ in r, θ and z directions are calculated using the plastic multiplier Λ for the S-CLAY1S model, which considers an associated flow rule.

$$\begin{Bmatrix} d\varepsilon_r^p \\ d\varepsilon_\theta^p \\ d\varepsilon_z^p \end{Bmatrix} = \Lambda \cdot \begin{Bmatrix} \dfrac{\partial f_y}{\partial \sigma_r'} \\ \dfrac{\partial f_y}{\partial \sigma_\theta'} \\ \dfrac{\partial f_y}{\partial \sigma_z'} \end{Bmatrix} \tag{19}$$

The plastic multiplier can be written in a matrix form as

$$\Lambda = \mathcal{H}\begin{bmatrix} \frac{\partial f_y}{\partial \sigma_r'} & \frac{\partial f_y}{\partial \sigma_\theta'} & \frac{\partial f_y}{\partial \sigma_z'} \end{bmatrix} \begin{Bmatrix} d\sigma_r' \\ d\sigma_\theta' \\ d\sigma_z' \end{Bmatrix} \tag{20}$$

where

$$\mathcal{H} = -\frac{1}{\mathcal{H}_0 + \mathcal{H}_\alpha + \mathcal{H}_\chi} \tag{21}$$

$$\mathcal{H}_0 = \frac{\partial f_y}{\partial p_{mi}'} \frac{\partial p_{mi}'}{\partial \varepsilon_v^p} \frac{\partial f_y}{\partial p'} \tag{22}$$

$$\mathcal{H}_\alpha = \left\{\frac{\partial f_y}{\partial \boldsymbol{\alpha}^d}\right\}^T \left[\left\{\frac{\partial \boldsymbol{\alpha}^d}{\partial \varepsilon_v^p}\right\} \cdot \langle\frac{\partial f_y}{\partial p'}\rangle + \left\{\frac{\partial \boldsymbol{\alpha}^d}{\partial \varepsilon_d^p}\right\} \cdot \sqrt{\frac{2}{3}\left\{\frac{\partial f_y}{\partial \boldsymbol{\sigma}'^d}\right\} \cdot \left\{\frac{\partial f_y}{\partial \boldsymbol{\sigma}'^d}\right\}}\right] \tag{23}$$

$$\mathcal{H}_\chi = \frac{\partial f_y}{\partial \chi}\left[\frac{\partial \chi}{\partial \varepsilon_v^p}\left|\frac{\partial f_y}{\partial p'}\right| + \frac{\partial \chi}{\partial \varepsilon_d^p}\sqrt{\frac{2}{3}\left\{\frac{\partial f_y}{\partial \boldsymbol{\sigma}'^d}\right\} \cdot \left\{\frac{\partial f_y}{\partial \boldsymbol{\sigma}'^d}\right\}}\right] \tag{24}$$

All required derivatives and the derivation of the plastic multiplier are presented in Appendixes I and II, respectively.

Using decomposition of the strain vector ($d\boldsymbol{\varepsilon} = d\boldsymbol{\varepsilon}^e + d\boldsymbol{\varepsilon}^p$) and Eqs. (16-24), the elasto-plastic constitutive equations in the form of compliance and stiffness matrixes can be derived as

$$\begin{Bmatrix} d\varepsilon_r \\ d\varepsilon_\theta \\ d\varepsilon_z \end{Bmatrix} = \begin{bmatrix} \frac{1}{E} + \mathcal{H}n_r^2 & -\frac{\nu}{E} + \mathcal{H}n_r n_\theta & -\frac{\nu}{E} + \mathcal{H}n_r n_z \\ -\frac{\nu}{E} + \mathcal{H}n_\theta n_r & \frac{1}{E} + \mathcal{H}n_\theta^2 & -\frac{\nu}{E} + \mathcal{H}n_\theta n_z \\ -\frac{\nu}{E} + \mathcal{H}n_z n_r & -\frac{\nu}{E} + \mathcal{H}n_z n_\theta & \frac{1}{E} + \mathcal{H}n_z^2 \end{bmatrix} \cdot \begin{Bmatrix} d\sigma_r' \\ d\sigma_\theta' \\ d\sigma_z' \end{Bmatrix} \tag{25}$$

$$\begin{Bmatrix} d\sigma_r' \\ d\sigma_\theta' \\ d\sigma_z' \end{Bmatrix} = \frac{1}{\Gamma}\begin{bmatrix} c_{11} & c_{12} & c_{13} \\ c_{21} & c_{22} & c_{23} \\ c_{31} & c_{32} & c_{33} \end{bmatrix} \cdot \begin{Bmatrix} d\varepsilon_r \\ d\varepsilon_\theta \\ d\varepsilon_z \end{Bmatrix} \tag{26}$$

All terms in Eq. (26) are defined in Appendix III.

2.5. Rotational hardening rule

As derived by Sivasithamparam and Castro (2018), the changes in the fabric components ($d\alpha_r^d$, $d\alpha_\theta^d$ and $d\alpha_z^d$) with the radial direction are

$$\frac{d\alpha_i^d}{dr} = \Phi_i \mathcal{H}\left(n_r \frac{d\sigma_r'}{dr} + n_\theta \frac{d\sigma_\theta'}{dr} + n_r \frac{d\sigma_z'}{dr}\right) \quad \text{for } i=r,\theta,z \tag{27}$$

where

$$\Phi_i = \omega\left(\left(\frac{3(\sigma_i'-p')}{4p'} - \alpha_i^d\right)\langle\frac{\partial f_y}{\partial p'}\rangle + \omega_d\left(\frac{(\sigma_i'-p')}{3p'} - \alpha_i^d\right)\sqrt{\frac{2}{3}\left\{\frac{\partial f_y}{\partial \boldsymbol{\sigma}'^d}\right\} \cdot \left\{\frac{\partial f_y}{\partial \boldsymbol{\sigma}'^d}\right\}}\right) \quad \text{for } i=r,\theta,z \tag{28}$$

2.6. Bonding and destructuration

The destructuration hardening law (Eq. 7) relates the degradation of bonding with plastic straining. In three-dimensions, the plastic strain increments $d\varepsilon_v^p$ and $d\varepsilon_d^p$ are defined as

$$d\varepsilon_v^p = \Lambda \frac{\partial f_y}{\partial p'} \tag{29}$$

$$d\varepsilon_d^p = \Lambda \sqrt{\frac{2}{3}\left\{\frac{\partial f_y}{\partial \boldsymbol{\sigma}'^d}\right\} \cdot \left\{\frac{\partial f_y}{\partial \boldsymbol{\sigma}'^d}\right\}} \tag{30}$$

Degradation of bonding along the radial direction can be obtained by substituting Eqs. (29-30) and Eq. (20) into Eq.(7).

$$\frac{d\chi}{dr} = \Omega\mathcal{H}\left(n_r \frac{d\sigma_r'}{dr} + n_\theta \frac{d\sigma_\theta'}{dr} + n_r \frac{d\sigma_z'}{dr}\right) \tag{31}$$

where

$$\Omega = \chi\xi\left(\langle\frac{\partial f_y}{\partial p'}\rangle + \xi_d \sqrt{\frac{2}{3}\left\{\frac{\partial f_y}{\partial \boldsymbol{\sigma}'^d}\right\} \cdot \left\{\frac{\partial f_y}{\partial \boldsymbol{\sigma}'^d}\right\}}\right) \tag{32}$$

2.7. Solution procedure

The radial and tangential strain increments can be defined in natural strain form as

$$d\varepsilon_r = -\frac{\partial(dr)}{\partial r} \text{ and } d\varepsilon_\theta = \frac{dr}{r} \tag{33}$$

where r and dr are position of a material particle in the radial direction and change in the position of that particle, respectively.

Under undrained and plane strain conditions, the volumetric and vertical strains are zero, i.e. $d\varepsilon_v = d\varepsilon_z = 0$. Thus, using Eq. (33), the strain increments are defined as

$$d\varepsilon_r = -d\varepsilon_\theta = \frac{dr}{r} \tag{34}$$

By substituting Eq. (34) into Eqs. (26,27,31), and applying plane strain conditions, i.e. $d\varepsilon_z = 0$, the following seven partial differential equations are found (3 corresponding to stress increments, 3 to rotation of the yield surface and 1 to destructuration)

$$\begin{aligned} &\frac{d\sigma_r'}{dr} - \frac{c_{11}-c_{12}}{\Gamma}\frac{1}{r} = 0 \\ &\frac{d\sigma_\theta'}{dr} - \frac{c_{21}-c_{22}}{\Gamma}\frac{1}{r} = 0 \\ &\frac{d\sigma_z'}{dr} - \frac{c_{31}-c_{32}}{\Gamma}\frac{1}{r} = 0 \end{aligned} \tag{35}$$

$$\begin{aligned} &\frac{d\alpha_r^d}{dr} - \frac{\Phi_r\mathcal{H}}{\Gamma}\left[n_r(c_{11}-c_{12}) + n_\theta(c_{21}-c_{22}) + n_r(c_{31}-c_{32})\right]\frac{1}{r} = 0 \\ &\frac{d\alpha_\theta^d}{dr} - \frac{\Phi_\theta\mathcal{H}}{\Gamma}\left[n_r(c_{11}-c_{12}) + n_\theta(c_{21}-c_{22}) + n_r(c_{31}-c_{32})\right]\frac{1}{r} = 0 \\ &\frac{d\alpha_z^d}{dr} - \frac{\Phi_z\mathcal{H}}{\Gamma}\left[n_r(c_{11}-c_{12}) + n_\theta(c_{21}-c_{22}) + n_r(c_{31}-c_{32})\right]\frac{1}{r} = 0 \end{aligned} \tag{36}$$

$$\frac{d\chi}{dr} - \frac{\Omega\mathcal{H}}{\Gamma}\left[n_r(c_{11}-c_{12}) + n_\theta(c_{21}-c_{22}) + n_r(c_{31}-c_{32})\right]\frac{1}{r} = 0 \tag{37}$$

The system of seven first-order ordinary differential equations (ODE) governs the expansion of the cylindrical cavity in the plastic region. Boundary conditions for the elasto/plastic boundary and the elastic solution (Appendix IV) are required for the complete mathematical formulation of the problem. As presented by Chen and Abousleiman (2012), the position of the material particle at the instant when the particle becomes plastic, $r_{xp,}$ can be obtained as

$$\frac{r_{xp}}{a} = \frac{2G_0}{2G_0-(\sigma_{rp}'-\sigma_{r0}')}\sqrt{\left(\frac{r_x}{a}\right)^2 + \left(\frac{a_0}{a}\right)^2 - 1} \tag{38}$$

The location of the current elastic/plastic interface r_p is the same as that for the S-CLAY1 model (Sivasithamparam and Castro 2018) because the natural yield surface is the same (Figure 2).

$$\frac{r_p}{a} = \sqrt{1-\left(\frac{a_0}{a}\right)^2} \bigg/ \sqrt{\frac{\sigma'_{rp} - \sigma'_{r0}}{G_0} - \left(\frac{\sigma'_{rp} - \sigma'_{r0}}{2G_0}\right)^2} \tag{39}$$

where

$$\sigma'_{zp} = \frac{3}{1+2K_0} p'_0$$

$$\sigma'_{rp} = \sigma'_{r0} + \sqrt{\frac{1}{3}\left(q^2 - (\sigma'_{z0} - K_0\sigma'_{z0})^2\right)} \tag{40}$$

$$\sigma'_{\theta p} = \sigma'_{\theta 0} - \sqrt{\frac{1}{3}\left(q^2 - (\sigma'_{z0} - K_0\sigma'_{z0})^2\right)}$$

where

$$\sigma'_{r0} = \sigma'_{\theta 0} = \frac{3K_0}{1+2K_0} p'_0 \text{ and } \sigma'_{z0} = \frac{3}{1+2K_0} p'_0 \tag{41}$$

and

$$q = \sqrt{q_0^2 + \left(\bar{q}^2 - (q_0 - \alpha p'_0)^2\right)} \tag{42}$$

where

$$q_0 = \sqrt{\frac{3}{2}\left((\sigma'_{r0} - p'_0)^2 + \left(\sigma'_{\theta 0} - p'_0\right)^2 + (\sigma'_{z0} - p'_0)^2\right)} \tag{43}$$

and

$$\bar{q} = \sqrt{(M^2 - \alpha_0^2)(p'_m - p'_0)p'} \tag{44}$$

The system of equations (Eqs. 35-37), imposing the boundary conditions (Eqs. 38-40), can be solved numerically; here, the standard differential solver 'lsode' available in GNU Octave v4.0 was used. Figure 3 summarizes the solution procedure.

The pore pressure distribution can be calculated by integration from the elastic/plastic interface up to the point r_x.

$$\Delta u = u(r_x) - u_0 = \sigma'_{rp} - \sigma'_r(r_x) - \int_{r_p}^{r_x} \frac{\sigma'_r - \sigma'_\theta}{r} \, dr \tag{45}$$

3. Results and Discussion

3.1. Validation

Validation of the proposed semi-analytical solution has been performed by comparison of its results with finite element simulations using the commercial code Plaxis 2D 2017 (Brinkgreve et al. 2017). The S-CLAY1S model has been implemented as User-defined soil model in Plaxis, using an automatic substepping in combination with a modified Newton-Raphson integration scheme (Sivasithamparam 2012; Sivasithamparam and Castro 2016.)

The geometrical model (Figure 4) is based on that used by González et al. (2009) for plane strain cylindrical cavity expansion. The boundary condition at the outer boundary is a fixed radial stress (equal to the initial value) and free radial displacements to deal with the material incompressibility (undrained conditions) in a model of finite dimensions. This geometrical model has proven to be more computationally efficient than the geometrical model used in Sivasithamparam and Castro (2018), which was based on that proposed by Burd and Houlsby (1990) using a correcting layer. Sensitivity analyses of mesh refinement, load step size and water bulk modulus were performed to confirm their small influence.

To account for large displacements, the numerical code uses an updated Lagrangian formulation (McMeeking and Rice 1975) and adopts the co-rotational rate of Kirchhoff stress (also known as Hill stress rate). The details of the implementation can be found in Van Langen (1991).

For the sake of comparison with previous studies, Boston blue clay (BBC) is considered and its Modified Cam clay (MCC) parameters are taken from Chen and Abousleiman (2012) and additional anisotropic parameters from Sivasithamparam and Castro 2018 (S-CLAY1) (see Table 1). Additional parameters for intrinsic compressibility, bonding and destructuration have been taken from the literature, just for illustrative purposes, without aiming to reach a detailed calibration of the parameters using experimental tests.

BBC is a moderately sensitive marine clay and, for example, Whittle et al. (1994) use a value of S_t=4.5. For the S-CLAY1S model, that implies χ_0=3.5 (Table 1). For parametric analyses, four times this value has also been used (χ_0=14). Cerato and Lutenegger (2004) obtained an intrinsic compressibility of BBC remoulded at 1.25 times the liquid limit of λ_i=0.12, which is slightly lower than the natural compressibility used in previous cavity expansion papers (λ=0.15) (e.g., Chen and Abousleiman 2012; Sivasithamparam and Castro 2018) and, thus, in agreement with the moderate sensitivity of BBC. Finally, the parameters of the destructuration hardening law (Eq. 7) are set equal to their default values (ξ=9 and ξ_d=0.2) (e.g., Karstunen et al. 2006)

The overconsolidation ratio (OCR) of BBC varies with depth. To provide a broad representation of different depths, several OCR values are considered, namely 1, 1.5, 3 and 5. Their corresponding initial state parameters are shown in Table 2 and are the same as in Sivasithamparam and Castro (2018) for the sake of comparison.

Values of undrained shear strength for plane strain conditions (Table 2) were numerically simulated. For cases without destructuration (χ_0=0) and triaxial compression conditions or normally consolidated conditions, the analytical expression may be found in Sivasithamparam and Castro (2018). When destructuration is considered, the undrained shear strength reduces towards a residual value that was analytically deduced here following a similar procedure as that used by Potts and Zdravkovic (1999) for MCC:

$$c_u = \frac{c_u(\chi_0=0)}{(1+\chi_0)^{1-\kappa/\lambda}} \tag{46}$$

Nevertheless, the residual value of the undrained shear strength is not commonly reached for usual ranges of strain. Therefore, it is not useful for practical purposes to normalize the results by the undrained shear strength as commonly done for models that do not considered destructuration (e.g., Randolph et al. 1979; Chen and Abousleiman 2012; Sivasithamparam and Castro 2018). Thus, results will be generally normalized by the initial vertical effective stress in this paper. In some special cases, values are normalized by the undrained shear strength (Table 2) to compare with analytical values.

Comparison between finite element simulations and the semi-analytical solution gives minor differences as may be observed in Figure 5 for the stresses around the cavity as an example.

3.2. Internal cavity pressure

To expand the cavity, an internal pressure (radial stress), σ_a, must be applied. Its value must monotonically increase to continue with the expansion of the cavity. When the cavity has been notably expanded (around $a/a_0>2$), σ_a approaches an asymptotic limit value, sometimes called pressuremeter limit pressure. Figure 6 shows its variation with the normalized cavity radius for different OCR and χ_0 values. Ambient pore pressures are not included because they are not relevant and could mask the results.

Excess pore pressures at the cavity wall (Δu_a) are depicted in Figure 7. For high OCR values, slight negative excess pore pressures could be generated at the beginning of the cavity expansion (small a/a_0 values).

González et al. (2009) pointed out that mechanical overconsolidation and initial bonding have similar effects on the load-displacement curve (Figure 6). Here, the same trends are found but the influence of the initial bonding is limited beyond values around $\chi_0>3.5$. That is because the smaller values of the effective radial stresses, when considering higher values of initial bonding, are nearly compensated by larger excess pore pressures (Figure 7). González et al. (2009) proposed to use unloading-reloading cycles or strain holding phases to try to distinguish between the effects of mechanical overconsolidation and initial bonding. If pore water pressures are measured at the cavity wall (e.g., when using the Cambridge self-boring pressuremeter), effective radial stress at the cavity wall (Figure 8) may be used to estimate the initial degree of bonding from the softening part. Nevertheless, field measurements may not clearly show the softening part (e.g., Hamouche et al. 1995).

When destructuration is not considered, the effective radial stress (Figure 8) quickly reaches a constant ultimate value (for $a/a_0>1.3$). For cases with destructuration, the effective radial stress continues decreasing for large cavity expansions, but also tends towards a constant ultimate value. In both cases and for any value of OCR and χ_0, there exists an analytical solution for the ultimate value of the effective radial stress ($\sigma'_r=(\sqrt{3}/M+1)c_u$).

3.3. Stresses around the cavity

Figure 9 shows the stresses and excess pore pressures around the cavity when the cavity radius is twice the initial one ($a/a_0=2$). For the sake of comparison, results for the case without destructuration (S-CLAY1, i.e. $\lambda=0.15$) (Sivasithamparam and Castro 2018) are also included in Figure 9. The extension of the plastic annulus depends on the OCR. For normally consolidated conditions, all the material points yield just when the cavity expansion begins, but plastic strains are not very important beyond $r>10a$.

Sivasithamparam and Castro (2018) showed that near the cavity the stresses are constant because the points are at critical state (CS) and the value of the stresses may be analytically obtained

$$\sigma'_r = (\sqrt{3}/M+1)c_u \quad ; \quad \sigma'_z = (\sqrt{3}/M)c_u \quad ; \quad \sigma'_\theta = (\sqrt{3}/M-1)c_u \tag{47}$$

Now, when destructuration is considered, Eq. (47) also holds, but CS is not usually reached for common expansions of the cavity (e.g., $a/a_0=2$) and common rates of destructuration (e.g., $\xi=9$ and $\xi_d=0.2$), because very large strains are necessary for a complete loss of structure (fully remoulded state). Thus, the values near the cavity are in a range between values given by Eq. (47) and $(1+\chi_0)^{1-\kappa/\lambda}$ times those values (Eq. 46).

3.4. Stress paths

For a better understanding of the problem, it is useful to observe the effective stress paths (ESP) followed by a point at the cavity wall during cavity expansion. Figures 10 and 11 show the stress paths for different OCR values in p'-q stress plane and π-plane, respectively. The stress paths illustrate the stress state of a point at the cavity wall from the beginning of the expansion (initial K_0 state) (a/a_0=1) until a final cavity expansion of a/a_0=2. Destructuration, i.e. loss of bonding, causes a gradual reduction of the yield surface towards the intrinsic yield surface. Destructuration is more important when the stress path has reached the critical state line (CSL) and plastic strains are larger. Then, the stress paths decrease along the CSL for plane strain conditions (Figures 10-12).

The initial yield surface (YS_0) plotted in Figure 10 corresponds to the triaxial plane, while yielding is here reached for a different value of the Lode's angle (Figure 11) (for further details, please refer to Sivasithamparam and Castro (2018) and Chen et al. in press).

Figure 12 depicts the influence of the initial amount of bonding (χ_0) on the stress paths. Higher values of χ_0 cause larger destructurations (Eq. 7), and consequently, lower final stresses and slightly faster changes of direction of the stress path.

Figure 11 also shows the path followed by the $\boldsymbol{\alpha}\cdot p'$ vector, which depicts the centre of the anisotropic yield surface. It shows how the yield surface rotates from triaxial compression conditions towards plane strain conditions. Destructuration causes a reduction of effective stresses (p'), but evolution of fabric anisotropy ($\boldsymbol{\alpha}$) is not influenced by destructuration, as it will be presented in the next section.

3.5. Fabric anisotropy

An interesting feature of this cavity expansion problem (incompressible material and plane strain conditions) is that the strain field may be first obtained, and then, the constitutive law is used to derive stresses. On the other hand, the evolution of fabric anisotropy is controlled by the corresponding hardening law (Eq. 6), which is the same for S-CLAY1 (model without destructuration) and S-CLAY1S (model with destructuration). Thus, the evolution of fabric anisotropy is exactly the same for both models.

Near the cavity, the fabric tensor reaches a constant value that may be analytically obtained as $\left[\alpha_r \quad \alpha_\theta \quad \alpha_z\right] = \left[1+\sqrt{3}M/9 \quad 1-\sqrt{3}M/9 \quad 1\right]$ (refer to Sivasithamparam and Castro (2018) for further details). Please, note that when destructuration is considered, large strains are necessary to reach CS, i.e. constant effective stresses and full loss of bonding, but the fabric tensor reaches much earlier a constant value that is the same as that at CS conditions.

3.6. Influence of structure and destructuration

Cavity expansion usually generates plastic strains, which in turn cause a loss of bonding of the structured clay (Figure 13) as per the assumed destructuration hardening law (Eq. 7). The loss of bonding (destructuration) is proportional to the current bonding parameter (Eq. 7). Consequently, the loss of bonding may be normalized by the initial amount of bonding in Figure 13.

Figure 13a shows the influence of OCR on the loss of bonding. It may be observed, that the loss of bonding at the cavity wall is independent of OCR, and only the extension of the plastic zone and, consequently, the extension of the zone where the amount of bonding decreases are influenced by OCR.

Larger radial expansions of the cavity generate larger soil distortions and larger destructuration of the soil, both in terms of extension and amount of destructuration (Figure 13b). The radial extension of destructuration is equal to the plastic annulus surrounding the cavity. Beyond a/a_0=10, the increase of r_p/a is negligible (Eq. 39). Results in Figure 13b for a/a_0=10 are nearly the same as for any other larger value. Please, note that this is for normalized values of the radius, r/a.

Figure 13c shows the influence of the rate of destructuration (ξ). Extreme values are chosen in Figure 13c to amply cover the range of possible values. ξ does not influence the plastic radius (r_p/a), but higher values of ξ obviously result in faster destructuration processes and lower final values of the bonding parameter.

The values of destructuration commented above are reflected on the stress distribution around the cavity. Thus, larger values of the imposed radial displacement generate larger extensions of the plastic annulus (r_p), higher excess pore pressures (Δu) and higher effective radial stresses (σ'_r) in the far field but lower values of σ'_r close to the cavity (Figure 14a). On the other hand, a faster rate of destructuration does not influence r_p, but leads to lower values of σ'_r near the cavity (Figure 14b). If the rate of destructuration is large enough (e.g., ξ=100 in this case), the points near the cavity wall reach CS and the effective stresses are constant in that CS annulus.

4. Comparison with experimental data

This section aims to highlight the capabilities of the proposed solution, but it does not consider a detailed example of practical application, which requires further investigation. A comparison is shown with data presented by Roy et al. (1981), who measured the variation of the undrained shear strength immediately after pile driving in a soft sensitive marine silty clay, namely Saint-Alban clay.

Saint-Alban clay has a critical state friction angle of 27° (e.g., Tavenas and Leroueil 1977). Following the approach proposed by Wheeler et al. (2003), anisotropic parameters were calculated (Table 3). Those anisotropic parameters agree with those used by Rezania et al. (2016), and some basic parameters, such as λ_i, e_0 and *OCR*, were taken from this reference. To illustrate the constitutive model capabilities and calibrate destructuration parameters, isotropically consolidated undrained (CIU) triaxial tests were simulated using S-CLAY1S (Figure 15) and compared with laboratory data (Tavenas and Leroueil 1977). A depth of circa 6 m was considered as representative and the corresponding initial state parameters (e.g., Roy et al. 1981; Rezania et al. 2016) are portrayed in Table 4.

To simulate the driving of piles in Saint-Alban clay, the radial expansion of a very small cylindrical cavity was considered using the proposed theoretical solution. Although a ratio $a/a_0 \geq 2$ may be enough in non-structured soils (e.g., Randolph et al. 1979), here a value of $a/a_0 \geq 10$ is necessary (e.g., Figure 8). The specific value of a does not influence the results, but in this case, it was $2a$=219 mm (Roy et al. 1981). The reduction of the normalized in situ vane strength immediately after pile driving measured by Roy et al. (1981) is shown in Figure 16. Estimations using the proposed theoretical solution are also included for comparison; c_u/c_{u0} was assumed as either proportional to p'/p'_0 or p'_m/p'_{m0}. The latter ratio is very similar to $(1+\chi)/(1+\chi_0)$.

For the comparison (Figure 16), several zones may be distinguished. At the pile shaft, the theoretical solution predicts a dramatic reduction of c_u, which is not measured in the field. Partial drainage may affect the measured value in the field at the pile shaft. At a distance between two and three pile radii, field measurements agree well with the theoretical solution. The reduction of c_u is between 10 and 40% and it is mainly caused by the loss of bonding. Other authors (e.g., Fellenius and Samson 1976; Bozozuk et al 1978) reported similar reductions of the in situ vane strength (around 15%) in the middles of pile groups. For r=4-7a, the theoretical values are slightly higher than those measured in the field and are influenced by the reduction of the mean effective stress (Figure 16). On the whole, the theoretical solution is able to predict the reduction of c_u immediately after pile driving.

5. Conclusions

A novel, exact and semi-analytical cylindrical cavity expansion solution for natural clays has been rigorously developed using the S-CLAY1S constitutive model, which is a Cam clay type of model that considers fabric anisotropy that evolves with plastic strains, structure and gradual degradation of bonding (destructuration) due to plastic straining. The solution involves the numerical integration of a system of seven first-order ordinary differential equations, three of them corresponding to the effective stresses in cylindrical coordinates, other three corresponding to the components of the fabric tensor and one corresponding to the amount of bonding.

The semi-analytical solution has been validated against finite element analyses, using Boston blue clay as the reference natural clay.

When destructuration is considered, i.e. using the S-CLAY1S model, the solution provides lower values of the effective radial stresses near the cavity wall than those obtained when destructuration is not considered (S-CLAY1). The lower values of the effective radial stresses are partially compensated by larger values of the excess pore pressures. The limit asymptotic value of the effective stresses at the cavity wall may be analytically obtained as a function of the undrained shear strength. However, very large strains are required to reach the analytical limit values.

Interestingly, evolution of fabric anisotropy does not depend on the initial amount of bonding and the rate of destructuration and the same values of fabric anisotropy are obtained with both S-CLAY1 and S-CLAY1S soil models. The initial vertical cross anisotropy caused by the soil deposition changes towards a radial cross anisotropy after cavity expansion.

For common values, the soil near the cavity does reach the CSL, but does not reach CS, i.e. full remoulding and a constant stress state. The loss of bonding extends along the plastic annulus surrounding the cavity (larger for larger OCR and imposed radial displacements), being the largest at the cavity wall and progressively decreasing until a null loss of bonding in the elastic zone. The loss of bonding simulated by the theoretical solution is able to reproduce approximately the reduction of c_u immediately after pile driving in sensitive clays, as illustrated for a case in Saint-Alban clay.

References

1. Bozozuk M, Fellenius BH, Samson L (1978) Soil disturbance from pile driving in sensitive clay. Can Geotech J 15(3):346-361.
2. Brinkgreve RBJ, Kumarswamy S, Swolfs WM, Foria F (2017) Plaxis 2D 2017 Manual. Plaxis bv, the Netherlands.
3. Burd HJ, Houlsby GT (1990) Finite element analysis of two cylindrical expansion problems involving nearly incompressible material behavior. Int J Num Anal Methods Geomech 14:351-366.
4. Callisto L, Rampello S (2004) An interpretation of structural degradation for three natural clays. Can Geotech J 41:392-407.
5. Castro J, Karstunen M (2010) Numerical simulations of stone column installation. Can Geotech J 47:1127-1138.
6. Cerato AB, Lutenegger AJ (2004) Determining intrinsic compressibility of fine-grained soils. J Geotech Geoenviron Eng 130:872-877.
7. Chen H, Li L, Li J, Wang H (2019) Stress transform method to undrained and drained expansion of a cylindrical cavity in anisotropic modified cam-clay soils. Comput Geotech 106:128-142.
8. Chen SL, Abousleiman YN (2012) Exact undrained elasto-plastic solution for cylindrical cavity expansion in modified Cam Clay soil. Géotechnique 62:447-456.
9. Chen SL, Liu K (2019) Undrained cylindrical cavity expansion in anisotropic critical state soils. Géotechnique 69:189-202.
10. Chen SL, Liu K, Castro J, Sivasithamparam N. Discussion of undrained cylindrical cavity expansion in anisotropic critical state soils. Géotechnique (in press). https://doi.org/10.1680/jgeot.18.D.009

11. Coop MR, Wroth CP (1989) Field studies of an instrumented model pile in clay. Géotechnique 39:679-696.
12. Deotti LOG, Karstunen M, Almeida MCF, Almeida MS (2017) Modeling of laboratory tests on Saint-Roch-de-l'achigan clay with S-CLAY1S model. Int J Geomech 17:06016018.
13. Fellenius BH, Samson L (1976) Testing of drivability of concrete piles and disturbance to sensitive clay. Can Geotech J 13(1):139-160.
14. Gibson RE, Anderson WF (1961) In situ measurement of soil properties with the pressuremeter. Civ Eng Publ Works Rev 56:615-618.
15. Gens A, Nova R (1993) Conceptual bases for a constitutive model for bonded soils and weak rocks. Proc, Int Symp Hard Soils–Soft Rocks, Athens, Greece, 485–494.
16. González N, Arroyo M, Gens A (2009) Identification of bonded clay parameters in SBPM tests: a numerical study. Soils Found 49:329-340.
17. Hamouche KK, Roy M, Leroueil S (1995) A pressuremeter study of Louiseville sensitive clay. Proc, 4th Int Symp Pressuremeter New Av (ed. Ballivy G). Balkema, Rotterdam. p. 361-366.
18. Karstunen M, Krenn H, Wheeler SJ, Koskinen M, Zentar R (2005) Effect of anisotropy and destructuration on the behaviour of Murro test embankment. Int J Geomech 5:87–97.
19. Karstunen M, Wiltafsky C, Krenn H, Scharinger F, Schweiger HF (2006) Modelling the behaviour of an embankment on soft clay with different constitutive models. Int J Numer Anal Meth Geomech 30:953-982.
20. Ladd CC, Germaine JT, Baligh MM, Lacasse SM (1980) Evaluation of self-boring pressuremeter tests in Boston blue clay. Federal Highway Administration, Report nº FHWA/RD-80/052. Nat. Tech. Info. Service, Springfield, Virginia, USA.

21. Li C, Zou J-F, Zhou H (in press) Cavity expansion in k0 consolidated clay. Eur J Enviro Civil Eng. https://doi.org/10.1080/19648189.2019.1605937

22. Li J, Gong W, Li L, Liu F (2017) Drained elastoplastic solution for cylindrical cavity expansion in K_0-consolidated anisotropic soil. J Eng Mech 143:04017133.

23. Li L, Li J, Sun D (2016) Anisotropically elasto-plastic solution to undrained cylindrical cavity expansion in K_0-consolidated clay. Comput Geotech 73:83-90.

24. Liu K, Chen SL (in press) Analysis of cylindrical cavity expansion in anisotropic critical state soils under drained conditions. Can Geotech J. dx.doi.org/10.1139/cgj-2018-0025.

25. McMeeking RM, Rice JR (1975) Finite-element formulation for problems of large elastic-plastic deformation. Int J Solids Struct 11:601-616.

26. Palmer AC (1972) Undrained plane-strain expansion of a cylindrical cavity in clay: A simple interpretation of the pressuremeter test. Géotechnique 22:451-457.

27. Prévost JH, Hoëg K (1975) Analysis of pressuremeter in strain softening soil. J Geotech Eng Div, ASCE 101:717-732.

28. Potts DM, Zdravkovic L (1999) Finite element analysis in geotechnical engineering: theory. Thomas Telford, London.

29. Randolph MF, Carter JP, Wroth CP (1979) Driven piles in clay-the effects of installation and subsequent consolidation. Géotechnique 29:361-393.

30. Rezania M, Taiebat M, Poletti E (2016) A viscoplastic SANICLAY model for natural soft soils. Comput Geotech 73:128-141.

31. Rouainia M, Muir Wood D (2000) A kinematic hardening constitutive model for natural clays with loss of structure. Géotechnique 50:153-164.

32. Roy M, Blanchet R, Tavenas F, La Rochelle P (1981) Behaviour of a sensitive clay during pile driving. Canadian Geotechnical Journal 18(2): 67-85.

33. Silvestri V (2003) Assessment of self-boring pressuremeter tests in sensitive clay. Can Geotech J 40:362-387.
34. Silvestri V, Tabib C (2018) Application of cylindrical cavity expansion in MCC model to a sensitive clay under K_0 consolidation. J Mater Civ Eng 30:04018155.
35. Sivasithamparam N (2012) Development and implementation of advanced soft soil models in finite elements. PhD thesis, University of Strathlcyde, Glasgow.
36. Sivasithamparam N, Castro J (2016) An anisotropic elastoplastic model for soft clays based on logarithmic contractancy. Int J Num Anal Methods Geomech 40:596-621.
37. Sivasithamparam N, Castro J (2018) Undrained expansion of a cylindrical cavity in clays with fabric anisotropy: theoretical solution. Acta Geotech 13: 729-746.
38. Tavenas F, Leroueil S (1977) Effects of stresses and time on yielding of clays. Proc 9th Int Conf Soil Mech Foundation Eng, Tokyo, Japan. p. 319-326.
39. Van Langen H (1991) Numerical analysis of soil-structure interaction. Ph.D. thesis, Delft University of Technology, Delft, the Netherlands.
40. Vesic AS (1972) Expansion of cavities in infinite soil mass. J Soil Mech Found Div, ASCE 98:265-290.
41. Wheeler SJ, Naatanen A, Karstunen M, Lojander M (2003) An anisotropic elastoplastic model for soft clays. Can Geotech J 40(2):403-418.
42. Whittle AJ, DeGroot DJ, Ladd CC, Seah T-H (1994) Model prediction of anisotropic behavior of Boston blue clay. J Geotech Eng 120: 199-224.
43. Yu HS (2000) Cavity expansion methods in geomechanics. Kluwer Academic, Dordrecht.

APPENDIX I: Derivatives

The partial derivatives used in the analytical solution are

$$\frac{\partial f_y}{\partial \sigma_i'} = \frac{p'\left(M^2-\alpha^2-\bar{\eta}^2\right)}{3} + \left(3s_i - s_r\alpha_r^d - s_\theta\alpha_\theta^d - s_z\alpha_z^d\right) \text{ for } i=r,\theta,z$$

where

$$\bar{\eta} = \frac{\bar{q}}{p'}$$

$$\bar{q} = \sqrt{\frac{3}{2}Q}$$

and

$$\frac{\partial f_y}{\partial p_{mi}'} = -p'(M^2-\alpha^2)(1+\chi)$$

$$\frac{\partial p_{mi}'}{\partial \varepsilon_v^p} = \frac{vp'}{(\lambda_i-\kappa)(1+\chi)(M^2-\alpha^2)}\left(M^2-\alpha^2+\bar{\eta}^2\right)$$

$$\frac{\partial f_y}{\partial p'} = p'(M^2-\alpha^2-\bar{\eta}^2) - 3(s_r\alpha_r^d + s_\theta\alpha_\theta^d + s_z\alpha_z^d)$$

$$\frac{\partial f_y}{\partial \alpha_i^d} = -3s_i p' + 3\alpha_i^d\frac{\bar{q}^2}{M^2-\alpha^2} \qquad \text{for } i=r,\theta,z$$

$$\frac{\partial f_y}{\partial \sigma_i'^d} = 3s_i \qquad \text{for } i=r,\theta,z$$

$$\frac{\partial \alpha_i^d}{\partial \varepsilon_v^p} = \omega\left(\frac{3(\sigma_i'-p')}{4p'} - \alpha_i^d\right) \qquad \text{for } i=r,\theta,z$$

$$\frac{\partial \alpha_i^d}{\partial \varepsilon_d^p} = \omega\omega_d\left(\frac{(\sigma_i'-p')}{3p'} - \alpha_i^d\right) \qquad \text{for } i=r,\theta,z$$

$$\sqrt{\frac{2}{3}\left\{\frac{\partial f_y}{\partial \boldsymbol{\sigma}'^d}\right\}\cdot\left\{\frac{\partial f_y}{\partial \boldsymbol{\sigma}'^d}\right\}} = 2\bar{q}$$

$$\frac{\partial f_y}{\partial \chi} = -\frac{p'^2}{(1+\chi)}\left[M^2-\alpha^2+\bar{\eta}^2\right]$$

$$\frac{\partial \chi}{\partial \varepsilon_v^p} = -\xi\chi$$

$$\frac{\partial \chi}{\partial \varepsilon_d^p} = -\xi\xi_d\chi$$

APPENDIX II: Derivation of the plastic multiplier

The consistency condition ($\dot{f}_y = 0$) is developed as:

$$\dot{f}_y = \frac{\partial f_y}{\partial \sigma_i'} d\sigma_i' + \frac{\partial f_y}{\partial p_{mi}'} dp_{mi}' + \frac{\partial f_y}{\partial \boldsymbol{\alpha}_d} d\boldsymbol{\alpha}_d + \frac{\partial f_y}{\partial \chi} d\chi = 0 \quad \text{for } i=r,\theta,z$$

and in terms of plastic strains, it is:

$$\dot{f}_y = \frac{\partial f_y}{\partial \sigma_i'} d\sigma_i' + \frac{\partial f_y}{\partial p_m'} \frac{\partial p_m'}{\partial \varepsilon_v^p} d\varepsilon_v^p + \frac{\partial f_y}{\partial \boldsymbol{\alpha}_d} \frac{\partial \boldsymbol{\alpha}_d}{\partial \varepsilon_v^p} \langle d\varepsilon_v^p \rangle + \frac{\partial f_y}{\partial \boldsymbol{\alpha}_d} \frac{\partial \boldsymbol{\alpha}_d}{\partial \varepsilon_d^p} \left| d\varepsilon_d^p \right| + \frac{\partial f_y}{\partial \chi} \frac{\partial \chi}{\partial \varepsilon_v^p} \langle d\varepsilon_v^p \rangle +$$

$$\frac{\partial f_y}{\partial \chi} \frac{\partial \chi}{\partial \varepsilon_d^p} \left| d\varepsilon_d^p \right| = 0 \quad \text{for } i=r,\theta,z$$

Thus, the plastic multiplier is

$$\Lambda = - \frac{\frac{\partial f_y}{\partial \sigma_i'} d\sigma_i'}{\frac{\partial f_y}{\partial p_{mi}'} \frac{\partial p_{mi}'}{\partial \varepsilon_v^p} \frac{\partial f_y}{\partial p'} + \left\{ \frac{\partial f_y}{\partial \boldsymbol{\alpha}_d} \right\}^T \left[\left\{ \frac{\partial \boldsymbol{\alpha}_d}{\partial \varepsilon_v^p} \right\} \cdot \langle \frac{\partial f_y}{\partial p'} \rangle + \left\{ \frac{\partial \boldsymbol{\alpha}_d}{\partial \varepsilon_d^p} \right\} \cdot \sqrt{\frac{2}{3} \left\{ \frac{\partial f_y}{\partial \boldsymbol{\sigma}_d'} \right\} \cdot \left\{ \frac{\partial f_y}{\partial \boldsymbol{\sigma}_d'} \right\}} \right] + \frac{\partial f_y}{\partial \chi} \left[\frac{\partial \chi}{\partial \varepsilon_v^p} \left| \frac{\partial f_y}{\partial p'} \right| + \frac{\partial \chi}{\partial \varepsilon_d^p} \sqrt{\frac{2}{3} \left\{ \frac{\partial f_y}{\partial \boldsymbol{\sigma}'^d} \right\} \cdot \left\{ \frac{\partial f_y}{\partial \boldsymbol{\sigma}'^d} \right\}} \right]}$$

APPENDIX III: Elasto-plastic solution

$$c_{11} = \frac{1}{E^2} \left(1 - \nu^2 + E\mathcal{H} n_\theta^2 + 2E\nu\mathcal{H} n_\theta n_z + E\mathcal{H} n_z^2 \right)$$

$$c_{12} = c_{21} = \frac{1}{E^2} \left[-E\mathcal{H}(n_\theta + \nu n_z) + \nu(1 + \nu - E\mathcal{H} n_\theta n_z + E\mathcal{H} n_z^2) \right]$$

$$c_{13} = c_{31} = \frac{1}{E^2} \left[-E\mathcal{H} n_r(\nu n_\theta + n_z) + \nu(1 + \nu - E\mathcal{H} n_\theta^2 + E\mathcal{H} n_\theta n_z) \right]$$

$$c_{22} = \frac{1}{E^2} (1 - \nu^2 + E\mathcal{H} n_r^2 + 2E\nu\mathcal{H} n_r n_z + E\mathcal{H} n_z^2)$$

$$c_{23} = c_{32} = \frac{1}{E^2} \left[\nu + \nu^2 + E\mathcal{H}\nu n_r^2 - E\mathcal{H} n_\theta n_z - E\mathcal{H}\nu n_r(n_\theta + n_z) \right]$$

$$c_{33} = \frac{1}{E^2} \left(1 - \nu^2 + E\mathcal{H} n_r^2 + 2E\nu\mathcal{H} n_r n_\theta + E\mathcal{H} n_\theta^2 \right)$$

$$\Gamma = -\frac{1+\nu}{E^3} \begin{bmatrix} (-1 + \nu + 2\nu^2) + E\mathcal{H}(-1 + \nu) n_r^2 + E\mathcal{H}(-1 + \nu) n_\theta^2 - \\ -2E\mathcal{H}\nu n_\theta n_z - E\mathcal{H} n_z^2 + E\mathcal{H}\nu n_z^2 - 2E\mathcal{H}\nu n_r(n_\theta + n_z) \end{bmatrix}$$

where

$$n_i = \frac{\partial f_y}{\partial \sigma_i'} \quad \text{for } i=r,\theta,z$$

APPENDIX IV: Elastic solution

The solution for the elastic total stresses (σ_r, σ_θ, σ_z) and the radial displacement (u_r) can be obtained imposing the assumption of null volumetric and vertical strains (for details see, for example, Yu 2000)

$$\sigma_r = \sigma_H + \left(\sigma_p - \sigma_H\right)\left(\frac{r_p}{r}\right)^2 \tag{IV.1}$$

$$\sigma_\theta = \sigma_H + \left(\sigma_p - \sigma_H\right)\left(\frac{r_p}{r}\right)^2 \tag{IV.2}$$

$$\sigma_z = \sigma_V \tag{IV.3}$$

$$u_r = \frac{\sigma_p - \sigma_H}{2G_0}\frac{r_p^2}{r} \tag{IV.4}$$

where σ_p is the total radial stress at the elasto/plastic boundary, σ_H and σ_V are the total horizontal and vertical stresses, respectively.

List of symbols

a	Radius of the cylindrical cavity
c_u	Undrained shear strength
$c_{u,PS}$	Undrained shear strength for plane strain conditions
$\boldsymbol{D}$	Elastic stiffness matrix
e	Void ratio
f_y	Function of the yield surface
G	Shear modulus
$K_{0\mathrm{NC}}$	Coefficient of lateral earth pressure at rest in normally consolidated conditions
K_0	Coefficient of lateral earth pressure
M	Slope of the critical state line
p'	Mean effective stress: $p' = \frac{(\sigma_r' + \sigma_\theta' + \sigma_z')}{3}$
p'_m	Size of the yield surface
p'_{mi}	Size of the intrinsic yield surface
q	Deviatoric stress: $q = \sqrt{\frac{1}{2}\left[\left(\sigma_r' - \sigma_\theta'\right)^2 + (\sigma_r' - \sigma_z')^2 + \left(\sigma_\theta' - \sigma_z'\right)^2\right]}$
$\bar{q}$	Invariant for anisotropic models. Radius of the yield surface in π-plane
Q	Invariant for anisotropic models: $Q = \frac{2}{3}\bar{q}^2$
S_t	Sensitivity
s	Deviatoric stress
u_r	Radial displacement

$\boldsymbol{\alpha}$	Fabric tensor
α	Inclination of the yield surface
$\boldsymbol{\alpha}_{\mathbf{d}}$	Deviatoric fabric tensor
Δ	Incremental operator
$\Delta\Lambda$	Plastic multiplier
ε	Strain
η	Stress ratio: $\eta=q/p'$ or $\boldsymbol{\eta}=\boldsymbol{\sigma}_{\mathbf{d}}/p'$ (tensor)
κ	Slope of swelling line from $\nu-\ln p'$ space
λ	Slope of the natural post yield compression line from $\nu-\ln p'$ space
λ_{i}	Slope of the intrinsic yield compression line from $\nu-\ln p'$ space
ν	Poisson's ratio
ξ, ξ_d	Absolute and relative effectiveness of plastic strains in destructuration
σ, σ'	Total and effective stresses
σ_a	Internal cavity pressure
σ_p	Total radial stress at the elastic/plastic boundary
υ	Specific volume
χ	Bonding parameter
ω, ω_d	Absolute and relative effectiveness of rotational hardening
CS	Critical state
CSL	Critical state line
ESP	Effective stress path
FEM	Finite element method
OCR	Overconsolidation ratio

YS	Yield surface

Subscripts/superscripts:

0	Initial
d,v	deviatoric, volumetric
H,V	horizontal, vertical
i	any of the axis components r, θ, z
p	plastic
r, θ, z	cylindrical coordinates

Bold notation is used for tensors.

Compressive stresses and strains are assumed as positive because it is the conventional sign notation in geotechnical engineering.

Table captions

Table 1. Soil properties, Boston blue clay.

Table 2. Soil state parameters and undrained shear strength, Boston blue clay.

Table 3. Soil properties, Saint-Alban clay.

Table 4. Soil state parameters and undrained shear strength, Saint-Alban clay.

Figure captions

Figure 1. Geometry of cylindrical cavity expansion: (a) cylindrical cavity; (b) horizontal cross section.

Figure 2. The S-CLAY1S natural and intrinsic yield surfaces in triaxial stress space and visualization of invariant $\bar{q}$.

Figure 3. Solution procedure for solving ordinary differential equations of cylindrical cavity expansion in GNU Octave.

Figure 4. Finite element model for cylindrical cavity expansion.

Figure 5. Validation of the theoretical solution against finite element analyses.

Figure 6. Radial stress at cavity wall during cavity expansion: (a) Influence of overconsolidation; (b) Influence of initial bonding.

Figure 7. Excess pore pressure at cavity wall during cavity expansion: (a) Influence of overconsolidation; (b) Influence of initial bonding.

Figure 8. Effective radial pressure at cavity wall during cavity expansion: (a) Normalized by the initial vertical effective stress; (b) Normalized by the undrained shear strength.

Figure 9. Influence of destructuration on stress distributions around the cavity: (a) OCR=1; (b) OCR=1.5; (c) OCR=5.

Figure 10. p'-q stress paths at cavity wall until a/a_0=2: (a) OCR=1; (b) OCR=1.5; (c) OCR=5.

Figure 11. Stress paths at cavity wall in π-plane until a/a_0=2: (a) OCR=1; (b) OCR=1.5; (c) OCR=5.

Figure 12. Influence of initial bonding on stress paths (until a/a_0=2). (a) p'-q plane; (b) π-plane.

Figure 13. Loss of bonding caused by cavity expansion: (a) Influence of OCR; (b) Influence of radial displacement; (c) Influence of rate of debonding.

Figure 14. Stress distributions around the cavity: (a) Influence of radial displacement; (b) Influence of rate of debonding.

Figure 15. Calibration of Saint-Alban clay parameters for S-CLAY1S using triaxial tests.

Figure 16. Variation of undrained shear strength immediately after pile driving in Saint-Alban clay. Comparison between field data and estimations using the theoretical solution.

Table 1. Soil properties, Boston blue clay.

Basic parameters				Anisotropy*			Destructuration			
κ	ν'	λ	M	α_0	ω	ω_d	χ_0	λ_i	ξ	ξ_d
0.03	0.278	0.15	1.2	0.46	80	0.76	3.5	0.12	9	0.2

*Following Wheeler et al. (2003)

Table 2. Soil state parameters and undrained shear strength, Boston blue clay.

OCR	σ'_{z0} (kPa)	K_0	e_0	G_0 (kPa)	$c_{u,PS}$ (kPa) λ=0.15 χ_0=0	$c_{u,PS}$ (kPa) λ=0.12 χ_0=0	$c_{u,PS}$ (kPa) λ=0.12 χ_0=3.5
1	160	0.5	1.09	3873	56.4	57.4	18.6
1.5	160	0.55	1.04	3969	78.7	78.7	25.5
3	120	0.71	1.00	3363	105.5	102.9	33.3
5	100	0.92	0.96	3223	137.0	130.9	42.4

Table 3. Soil properties, Saint-Alban clay.

Basic parameters**				Anisotropy***			Destructuration*		
κ *	ν'	λ_i	M	α_0	ω	ω_d	χ_0	ξ	ξ_d
0.04	0.3	0.25	1.07	0.41	40	0.6	9	15	0.3

* Calibration using triaxial data (Figure 15)

** Based on Rezania et al. (2016)

***Following Wheeler et al. (2003)

Table 4. Soil state parameters and undrained shear strength, Saint-Alban clay.

Depth (m)	OCR	σ'_{z0} (kPa)	$K_{0,NC}$	K_0	e_0	$c_{u,TX}$ (kPa)	$c_{u,PS}$ (kPa)
ca. 6	2	35	0.55	0.75	1.8	22.3	25.7

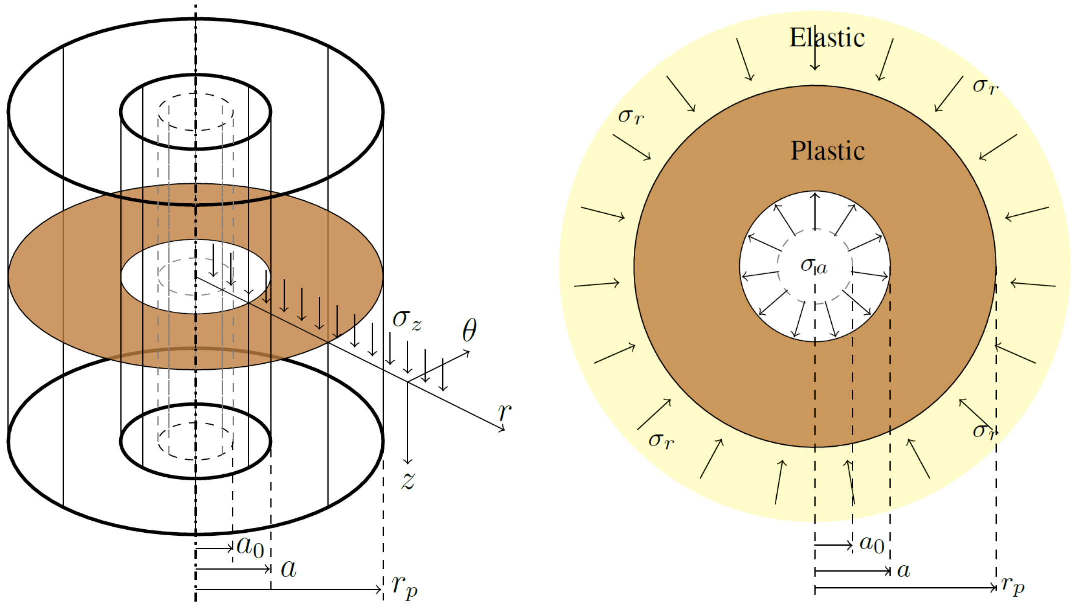

(a) (b)

Figure 1. Geometry of cylindrical cavity expansion: (a) cylindrical cavity; (b) horizontal cross section.

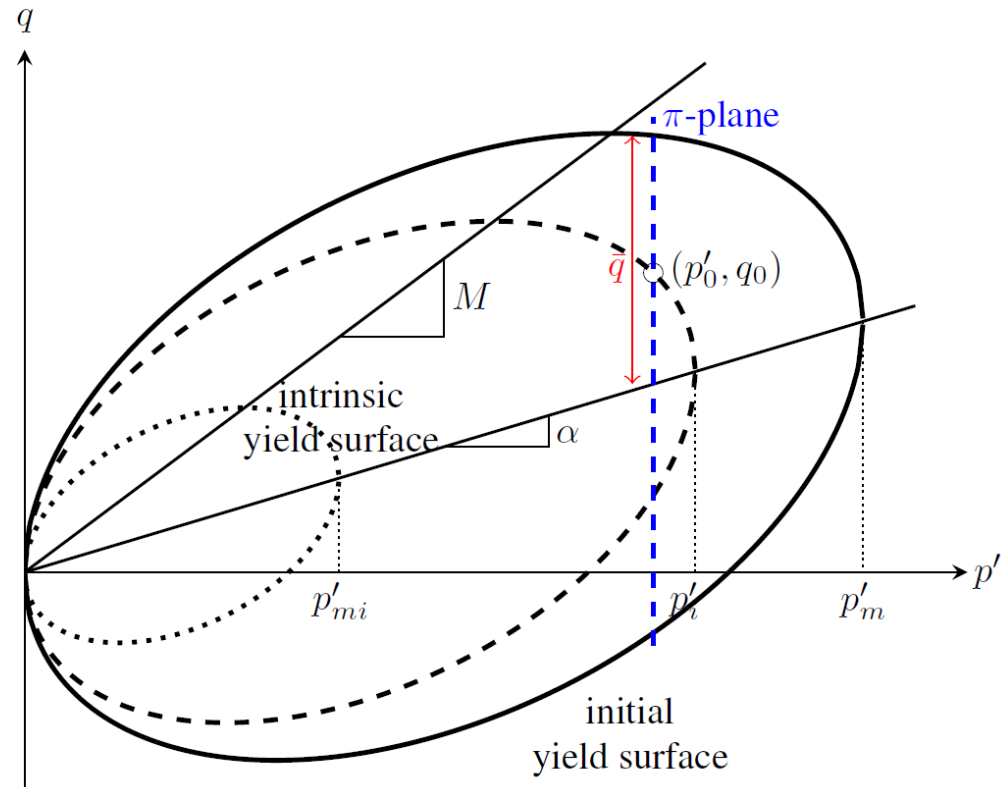

Figure 2. The S-CLAY1S natural and intrinsic yield surfaces in triaxial stress space and visualization of invariant $\bar{q}$.

```
Data: initial stress state, model parameters and $a/a_0$
Set initial anisotropic components ($\alpha_r, \alpha_\theta$ and $\alpha_z$)
Set initial bonding ($\chi = \chi_0$)
Determine stresses at initial yield ($\sigma'_{rp}$ , $\sigma'_{\theta p}$ , and $\sigma'_{zp}$ )
Determine elasto/plastic boundary ($r_p$)
Set initial ${}^{r_x}/_a = 1$
While ($i \leq nstep$)
        Solve ${}^{r_{xp}}/_a$ for given $a/a_0$, ${}^{r_x}/_a$, $\sigma'_{rp}$ , $\sigma'_{\theta p}$ , $\sigma'_{zp}$ and $G_0$
        Set interval $\left\{{}^{R_x}/_a\right\} = linspace\left({}^{r_{xp}}/_a , {}^{r_x}/_a , inc.\right)$
        Solve partial differential equation:
        $Y(\sigma, \alpha)$= lsode$\Big($ "ODE", $\left(\sigma'_{rp} , \sigma'_{\theta p}, \sigma'_{zp} ,\ \alpha_r, \alpha_\theta \text{ and } \alpha_z\right)$, $\left\{{}^{R_x}/_a\right\}$ $\Big)$
        lsode:
                function $ydot = ODE\ (Y, \{R_x/a\})$
                7.1.   Obtain:
                       $[\sigma'_r\ \ \sigma'_\theta\ \ \sigma'_z\ \ \alpha_r\ \ \alpha_\theta\ \ \alpha_z] = Y$
                7.2.   Calculate:
                       $\alpha_i^d$ for $i$=$r$,$\theta$,$z$ and $\alpha$
                       $p', G, E'$
                       $\frac{\partial f_y}{\partial \sigma'_i}$ for $i$=$r$,$\theta$,$z$ and hardening modulus $\mathcal{H}$
                       $c_{11}, c_{12}, c_{13}, c_{22}, c_{23}, c_{33}$ and $\Gamma$
                       $\Phi_i$ for $i$=$r$,$\theta$,$z$
                       $\Omega$ degradation of bonding
                7.3    Compute:
                       ${}^{d\sigma'_r}/_{dr}$ , ${}^{d\sigma'_\theta}/_{dr}$ and ${}^{d\sigma'_z}/_{dr}$
                       ${}^{d\alpha_r^d}/_{dr}$ , ${}^{d\alpha_\theta^d}/_{dr}$ and ${}^{d\alpha_z^d}/_{dr}$
                       $\frac{d\chi}{dr}$
                endfunction
        Update ${}^{r_x}/_a \leftarrow {}^{r_x}/_a + {}^{\Delta r}/_a$ $\left({}^{\Delta r}/_a = \left({}^{r_p}/_a - 1\right)/nstep\right)$
               $i \leftarrow i + 1$
        Get $\sigma'_r , \sigma'_\theta, \sigma'_z ,\ \alpha_r, \alpha_\theta$ and $\alpha_z$ from $Y(\sigma, \alpha)$
End
Calculate excess pore pressure $\Delta u$
If (OCR > 1) Calculate elastic stresses
End
```

Figure 3. Solution procedure for solving ordinary differential equations of cylindrical cavity expansion in GNU Octave.

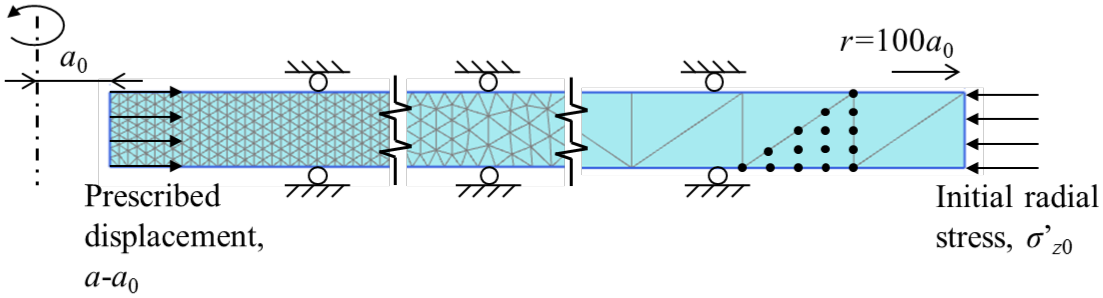

Figure 4. Finite element model for cylindrical cavity expansion.

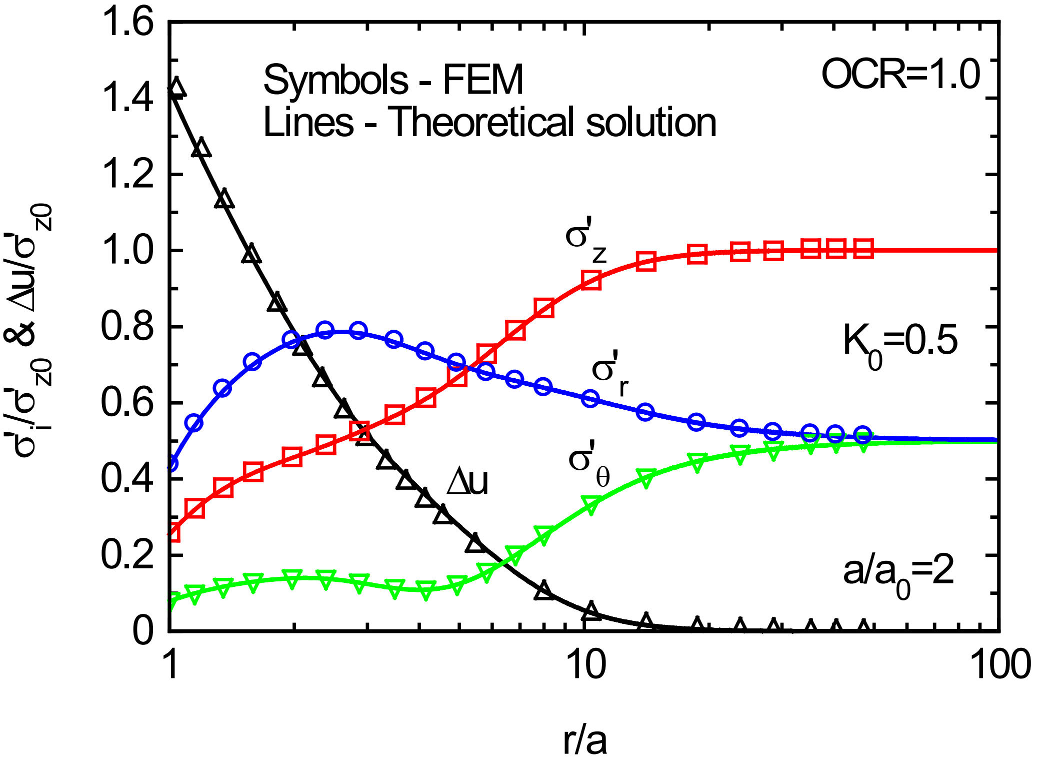

Figure 5. Validation of the theoretical solution against finite element analyses.

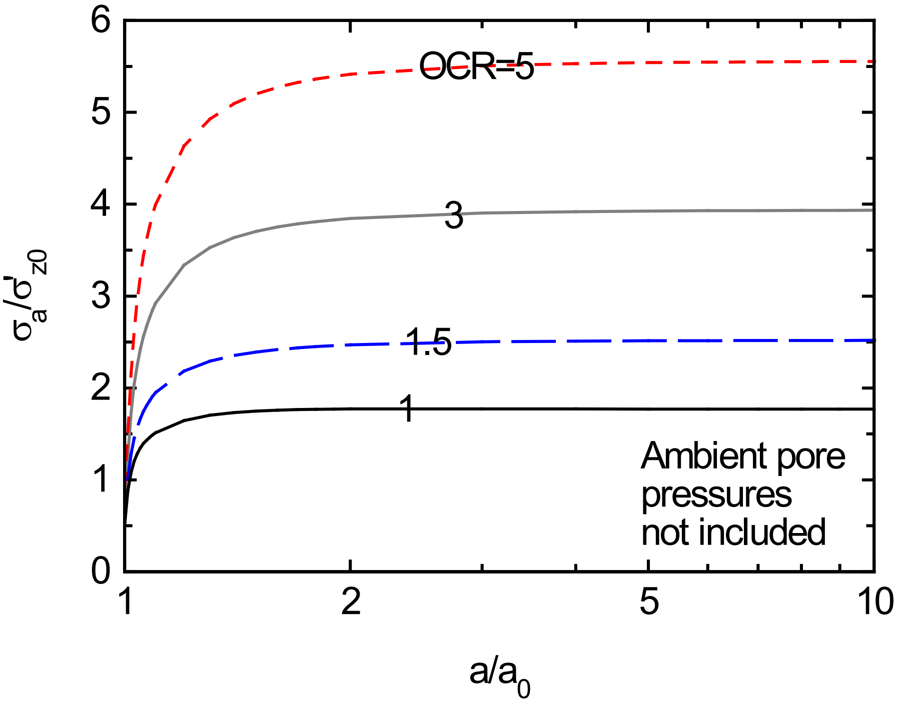

(a)

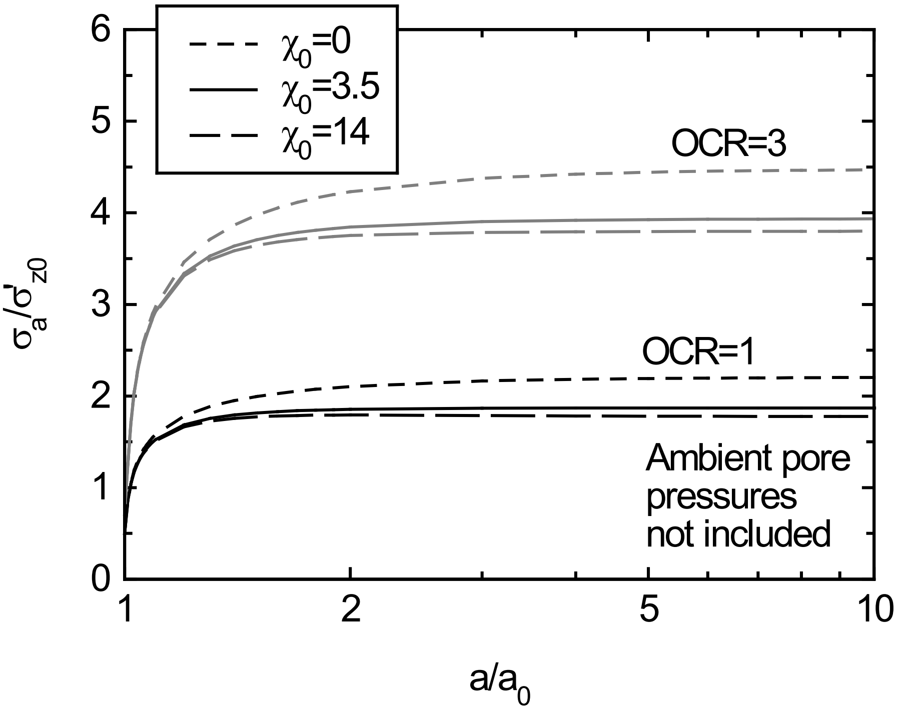

(b)

Figure 6. Radial stress at cavity wall during cavity expansion: (a) Influence of overconsolidation; (b) Influence of initial bonding.

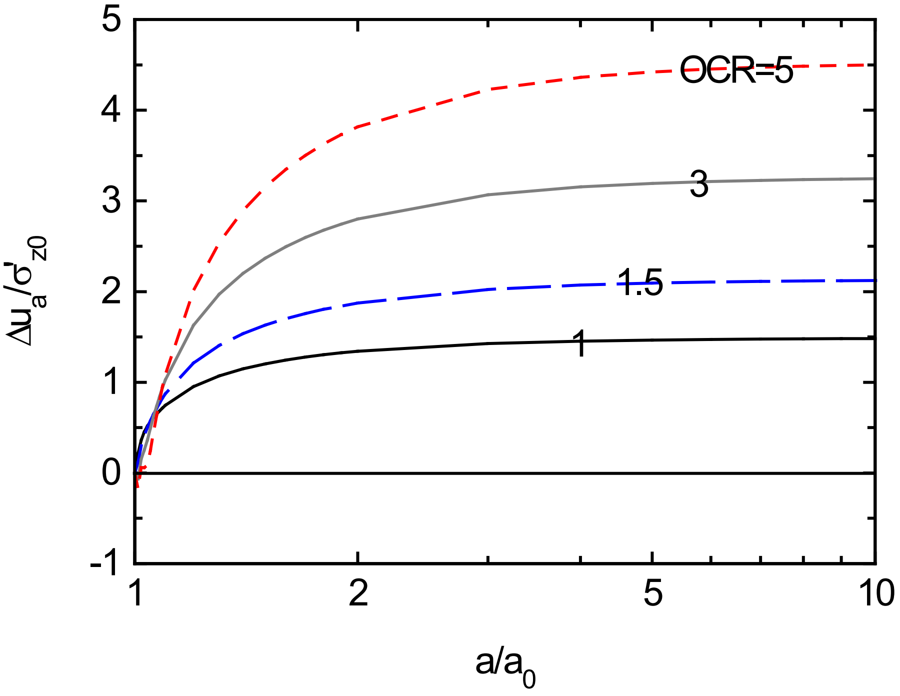

(a)

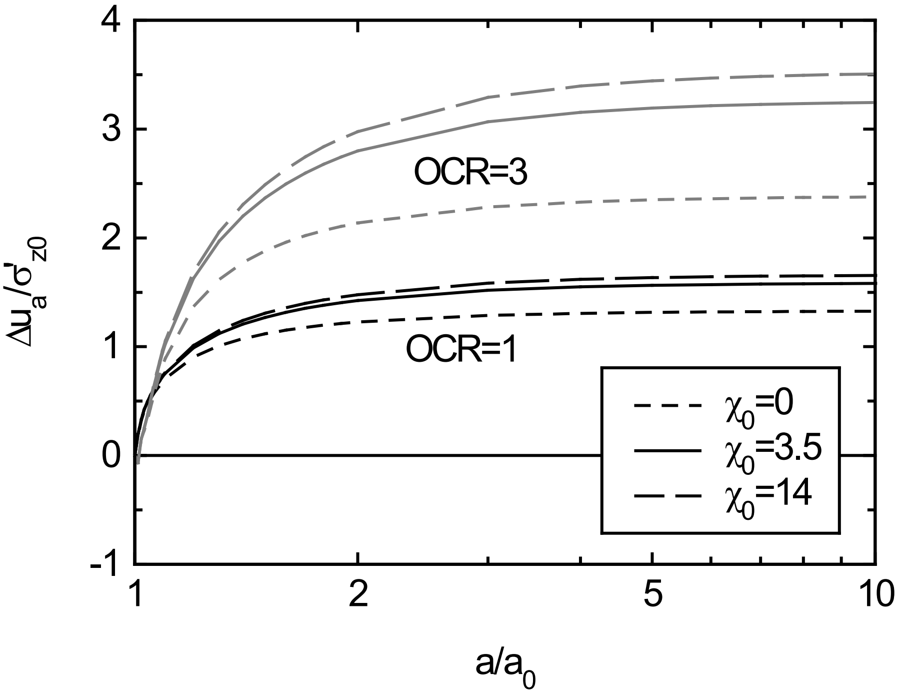

(b)

Figure 7. Excess pore pressure at cavity wall during cavity expansion: (a) Influence of overconsolidation; (b) Influence of initial bonding.

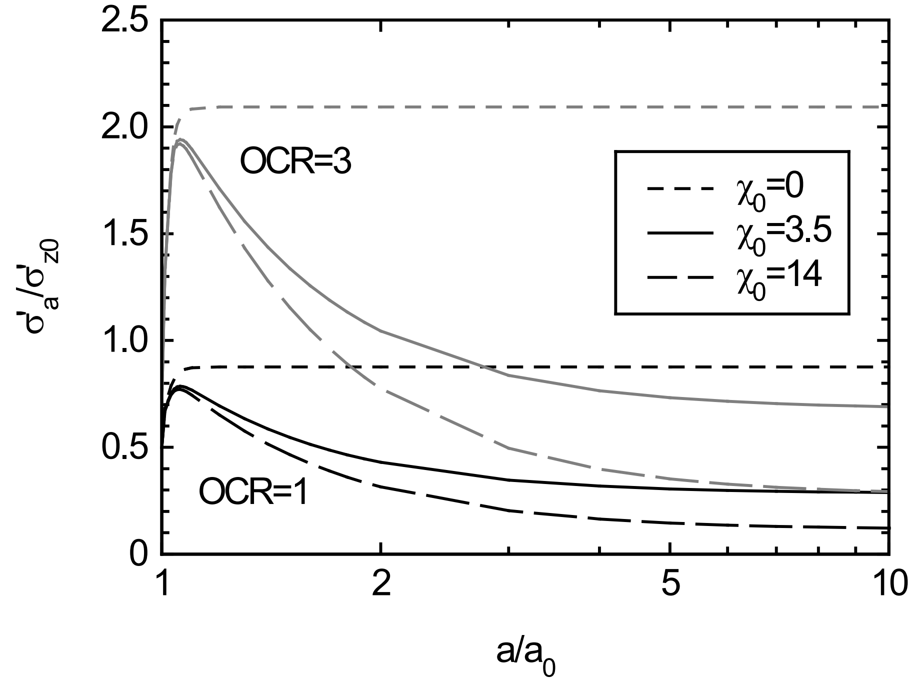

(a)

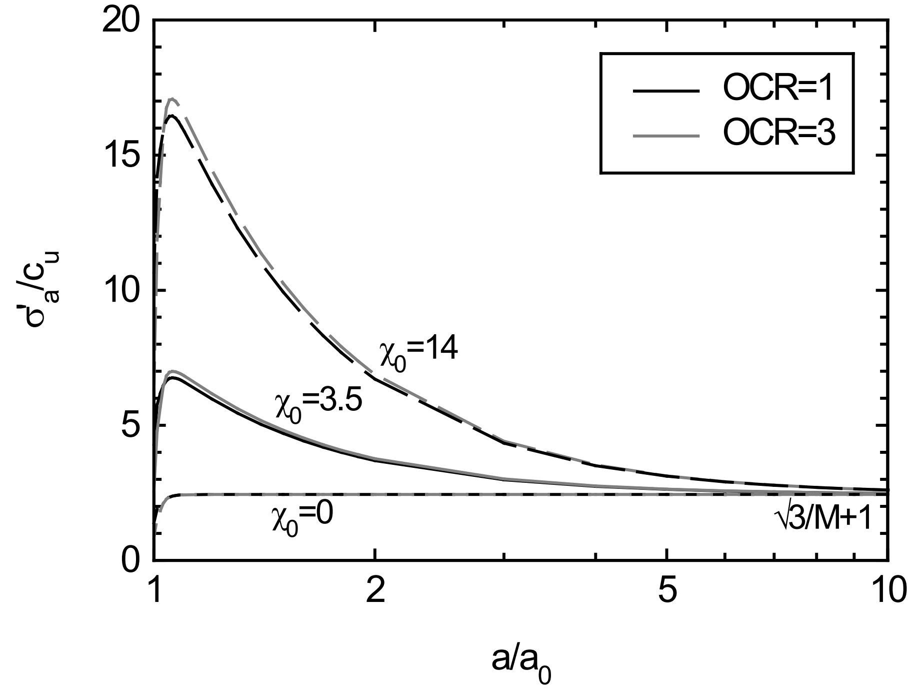

(b)

Figure 8. Effective radial pressure at cavity wall during cavity expansion: (a) Normalized by the initial vertical effective stress; (b) Normalized by the undrained shear strength.

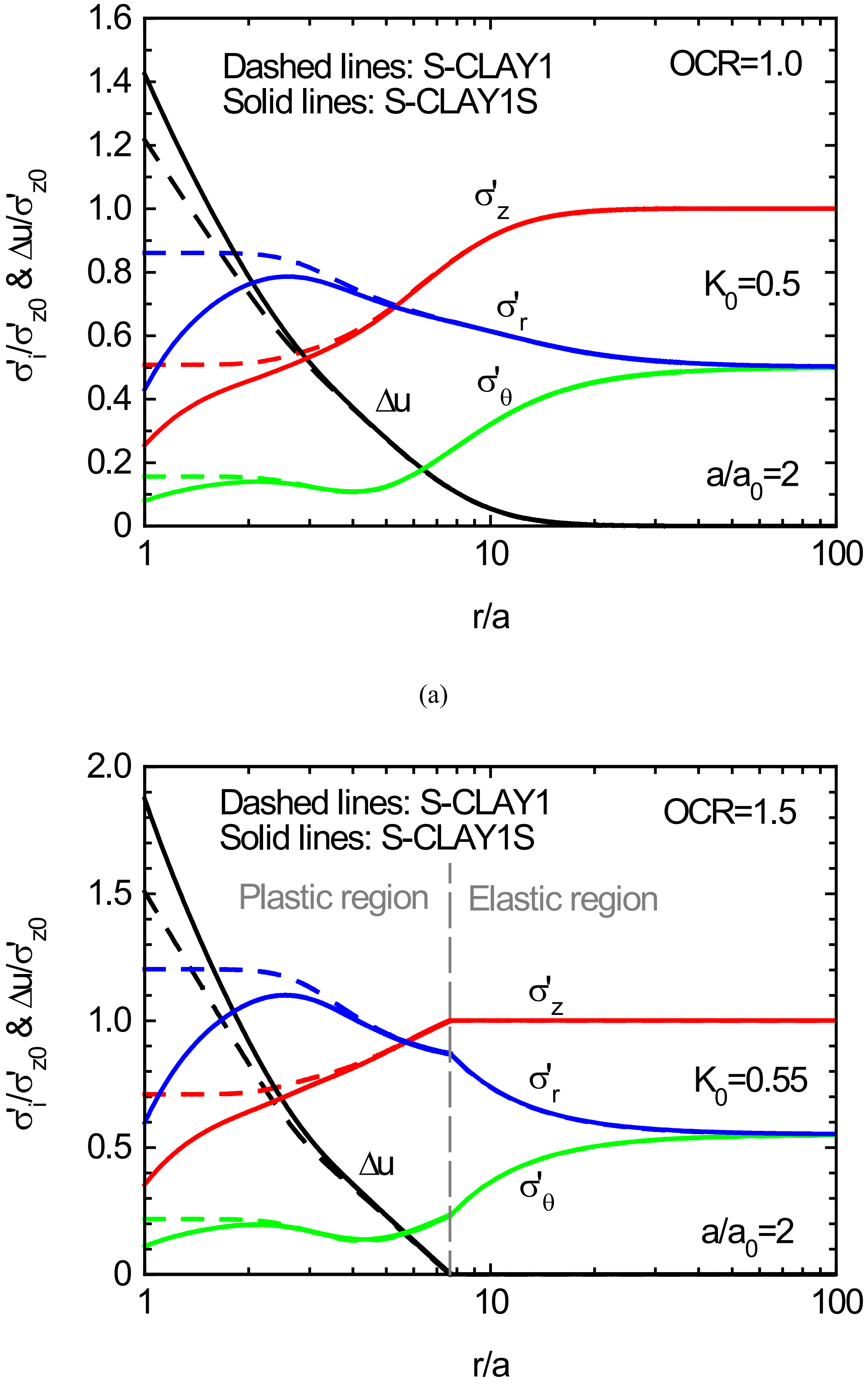
Dashed lines: S-CLAY1
Solid lines: S-CLAY1S
OCR=1.0
K0=0.5
a/a0=2
σ'z
σ'r
σ'θ
Δu
σ'i/σ'z0 & Δu/σ'z0
r/a
1.6
1.4
1.2
1.0
0.8
0.6
0.4
0.2
0
1
10
100
Dashed lines: S-CLAY1
Solid lines: S-CLAY1S
OCR=1.5
Plastic region
Elastic region
K0=0.55
a/a0=2
σ'z
σ'r
σ'θ
Δu
σ'i/σ'z0 & Δu/σ'z0
r/a
2.0
1.5
1.0
0.5
0
1
10
100

(a)

(b)

F.8

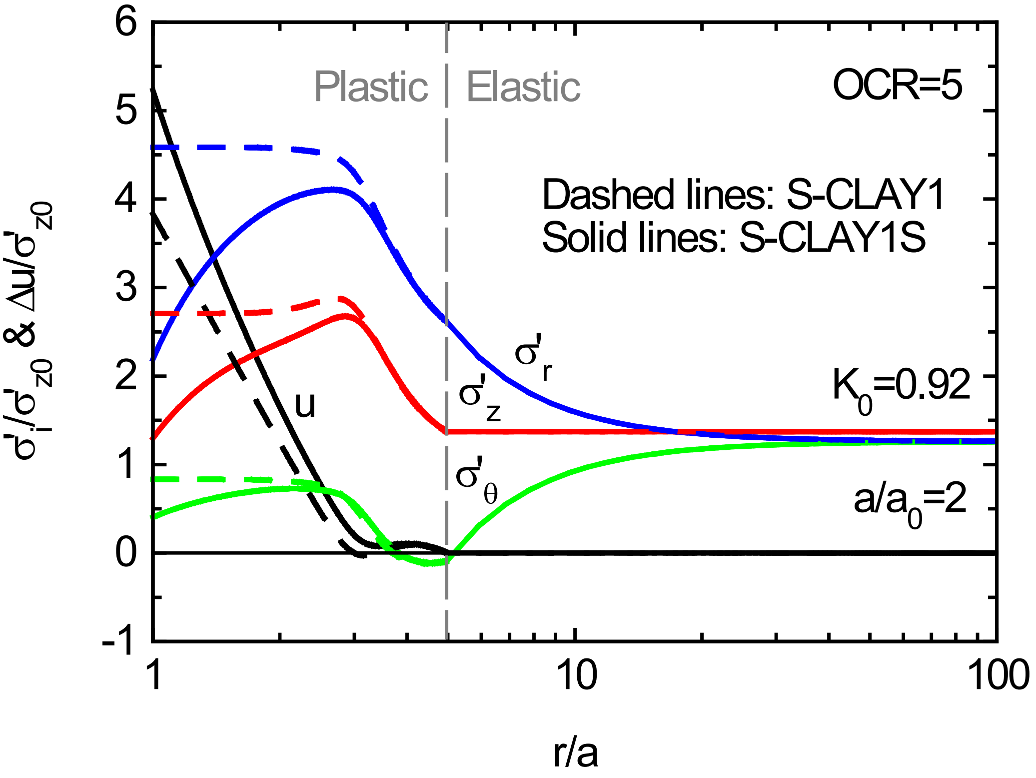

(c)

Figure 9. Influence of destructuration on stress distributions around the cavity: (a) OCR=1; (b) OCR=1.5; (c) OCR=5.

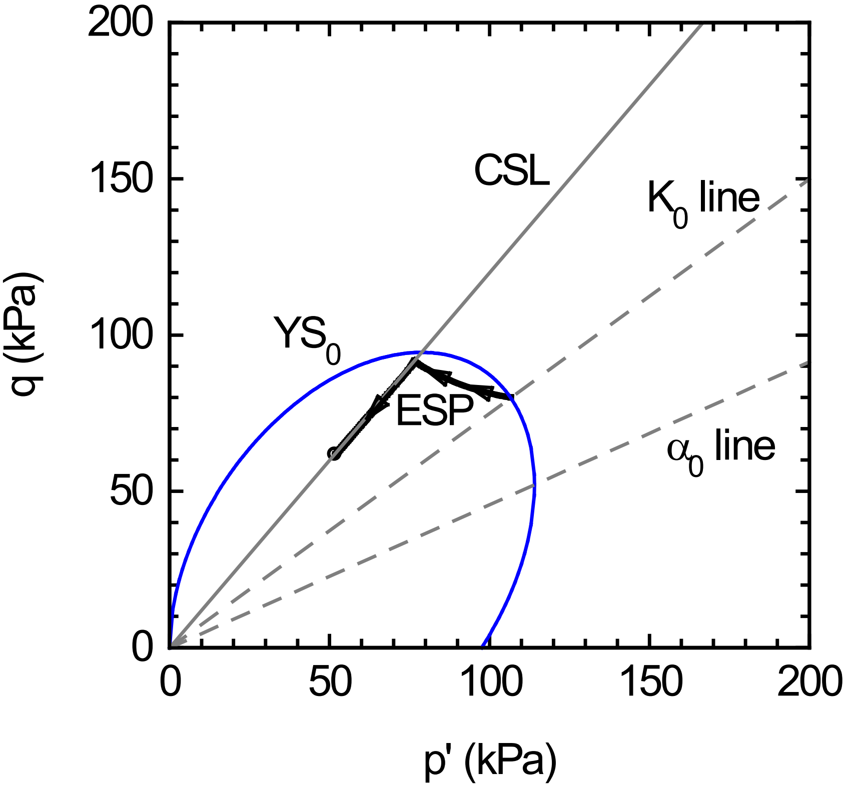

200
150
100
50
0
0
50
100
150
200
q (kPa)
p' (kPa)
CSL
K_0 line
YS_0
ESP
α_0 line

(a)

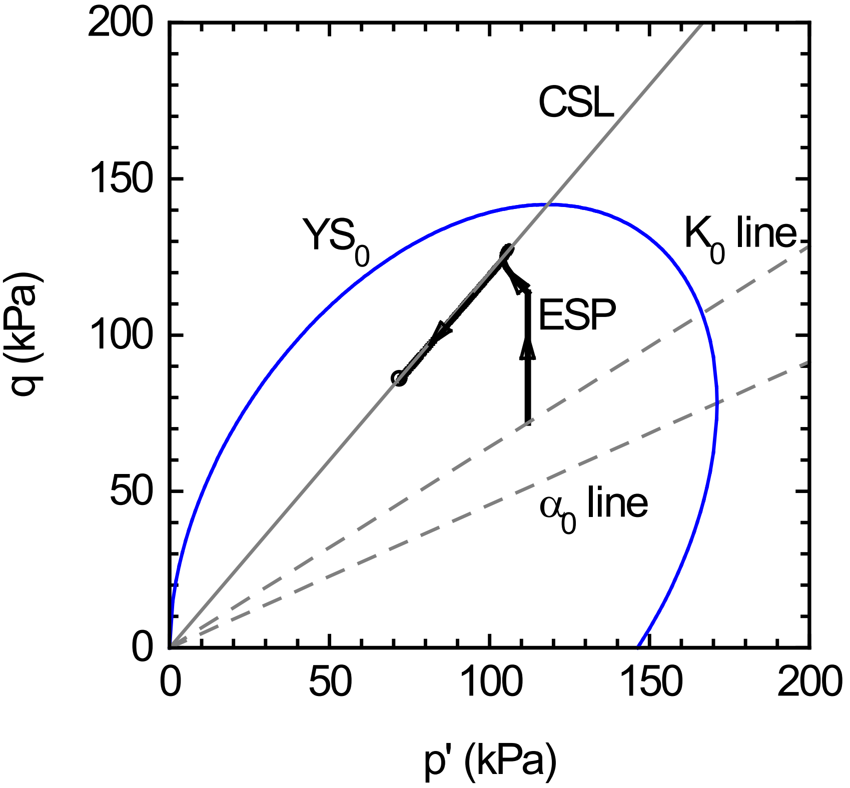

200
150
100
50
0
0
50
100
150
200
q (kPa)
p' (kPa)
CSL
YS_0
K_0 line
ESP
α_0 line

(b)

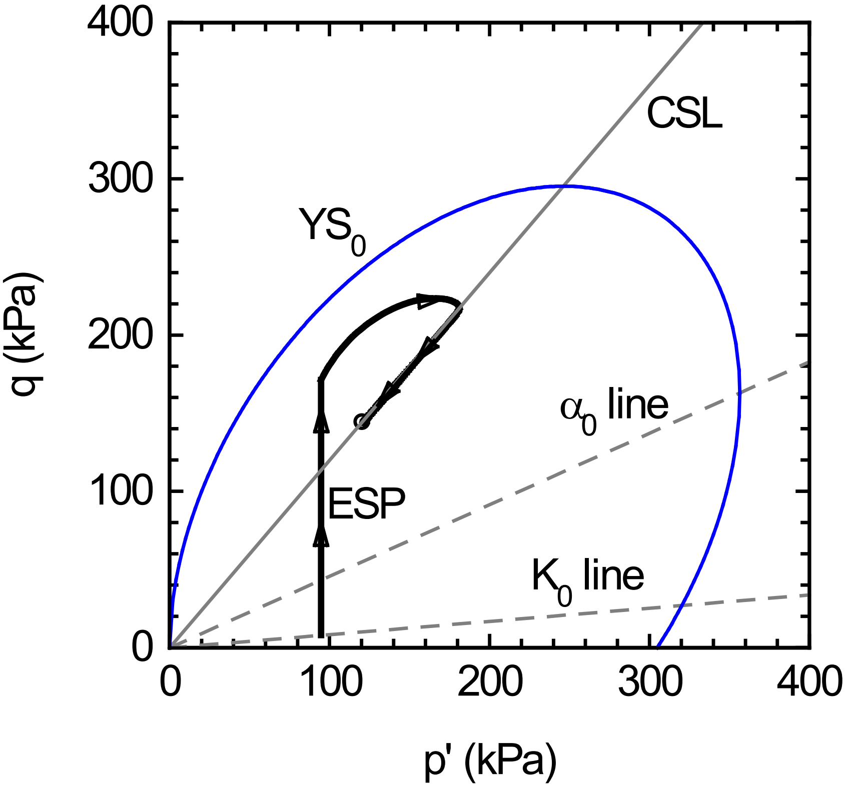

(c)

ESP: Effective stress path
CSL: Critical state line
YS_0: Initial Yield Surface in triaxial plane

Figure 10. *p*’-*q* stress paths at cavity wall until a/a_0=2: (a) OCR=1; (b) OCR=1.5; (c) OCR=5.

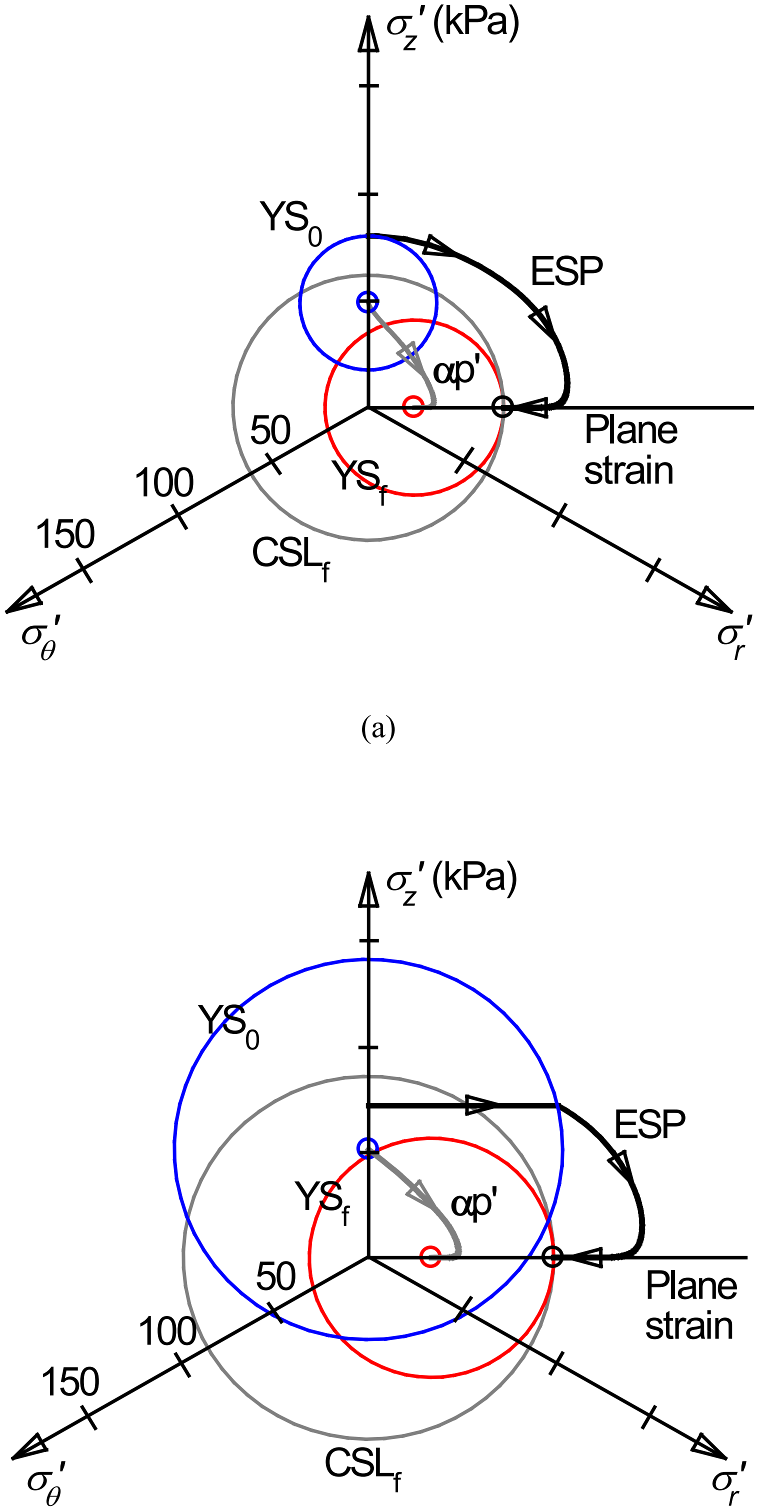
σz' (kPa)
YS0
ESP
αp'
Plane strain
50
100
150
YSf
CSLf
σθ'
σr'
σz' (kPa)
YS0
ESP
YSf
αp'
50
100
150
Plane strain
CSLf
σθ'
σr'

(a)

(b)

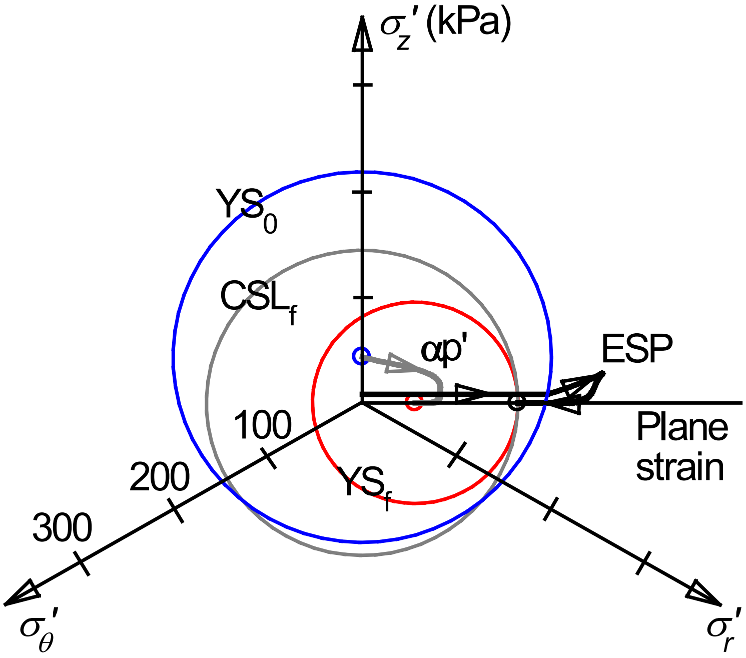

(c)

ESP: Effective stress path
CSL$_f$: Critical State Surface at failure
YS$_0$: Initial Yield Surface
YS$_f$: Final Yield Surface

Figure 11. Stress paths at cavity wall in π-plane until a/a_0=2: (a) OCR=1; (b) OCR=1.5; (c) OCR=5.

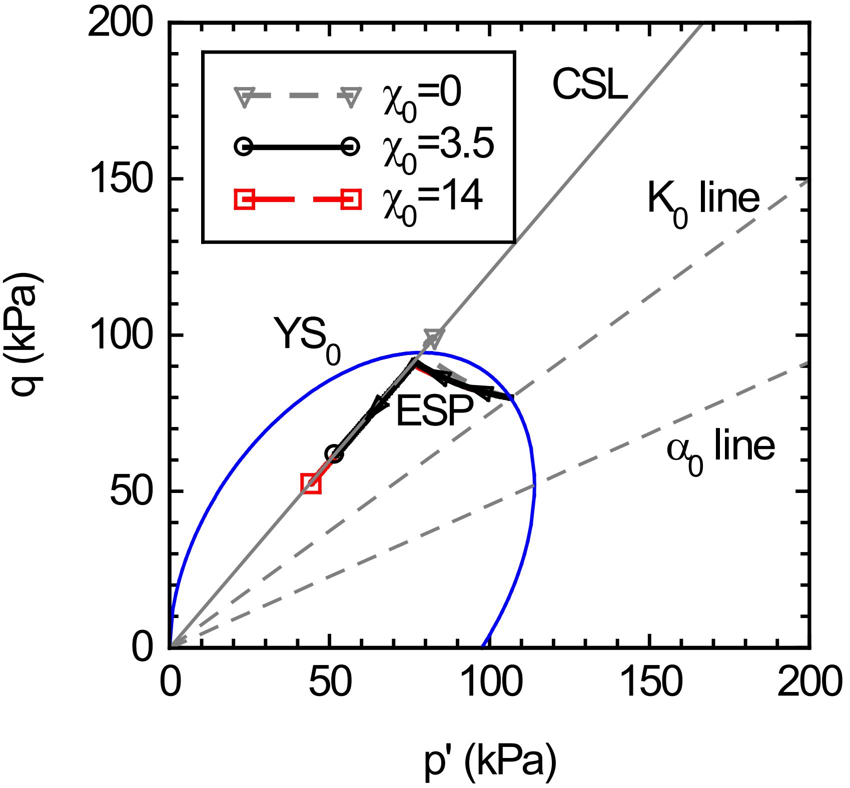

(a)

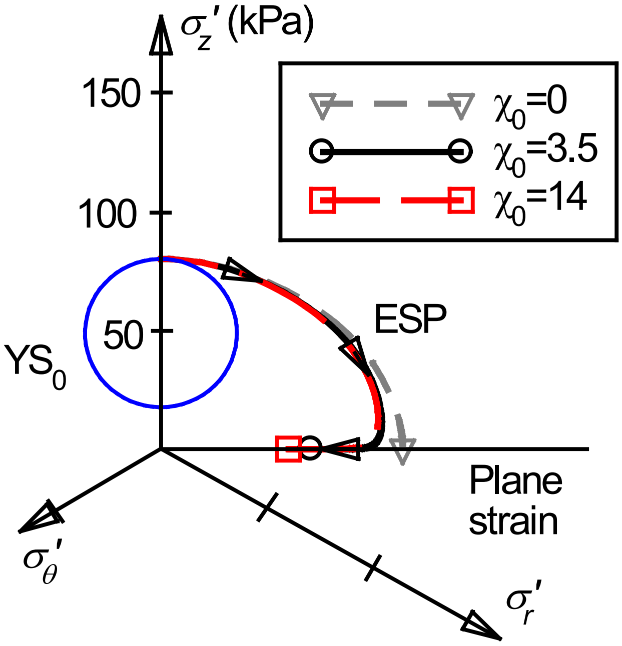

(b)

Figure 12. Influence of initial bonding on stress paths (until a/a_0=2). (a) p'-q plane; (b) π-plane.

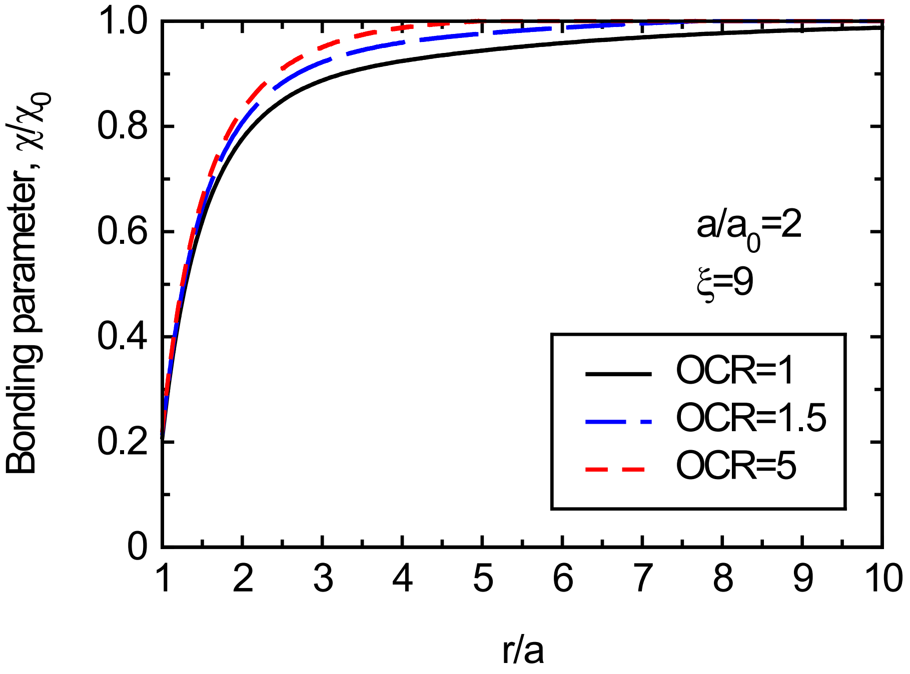
Bonding parameter, χ/χ_0
1.0
0.8
0.6
0.4
0.2
0
1
2
3
4
5
6
7
8
9
10
r/a
a/a_0=2
ξ=9
OCR=1
OCR=1.5
OCR=5

(a)

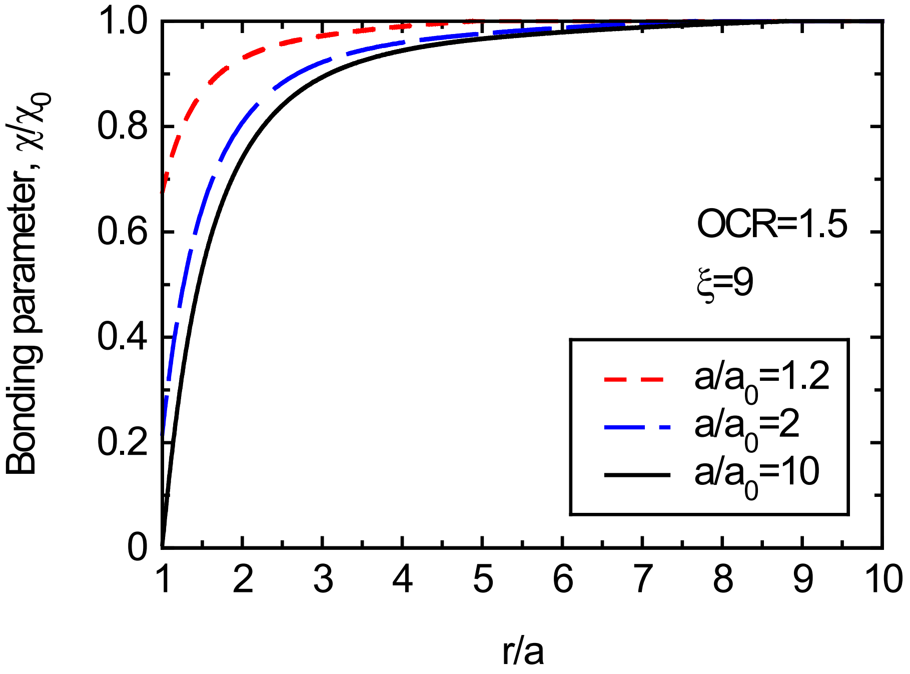
Bonding parameter, χ/χ_0
1.0
0.8
0.6
0.4
0.2
0
1
2
3
4
5
6
7
8
9
10
r/a
OCR=1.5
ξ=9
a/a_0=1.2
a/a_0=2
a/a_0=10

(b)

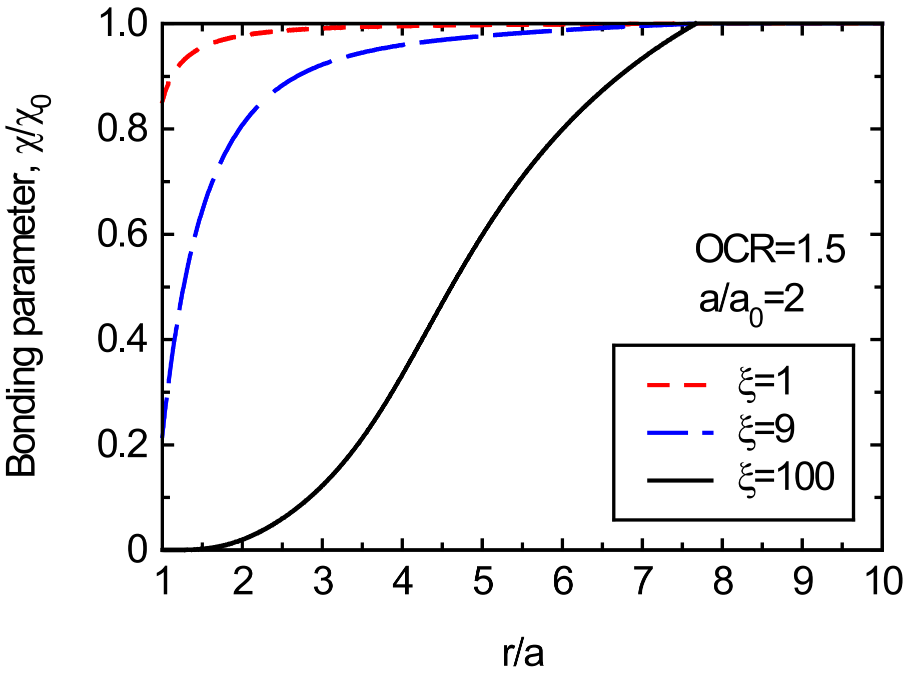

(c)

Figure 13. Loss of bonding caused by cavity expansion: (a) Influence of OCR; (b) Influence of radial displacement; (c) Influence of rate of debonding.

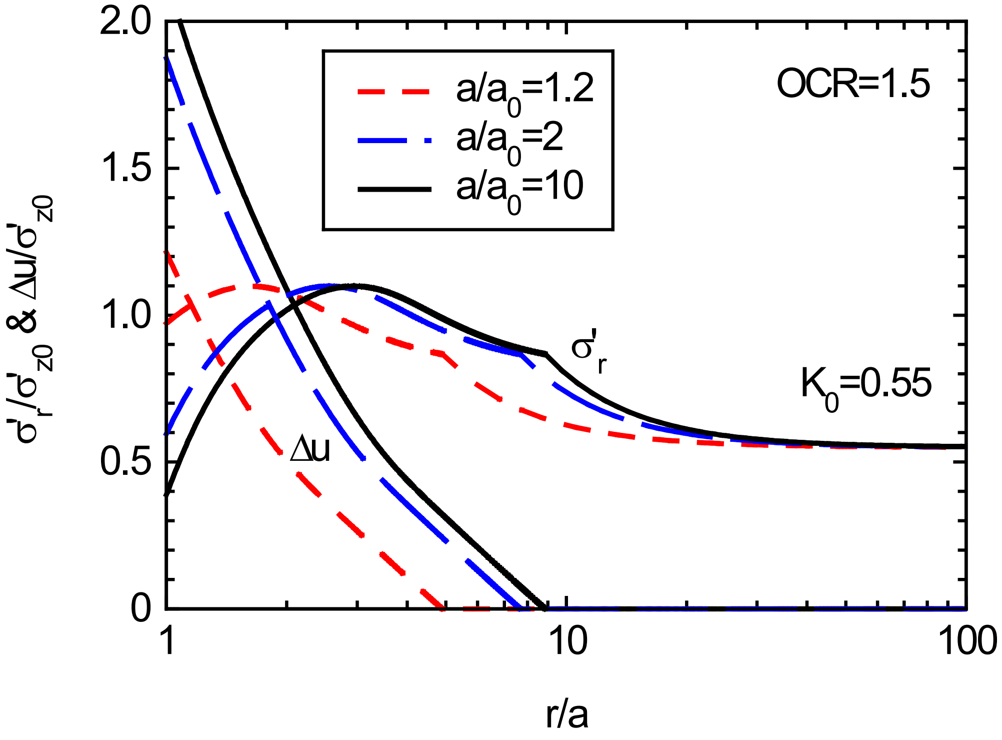

(a)

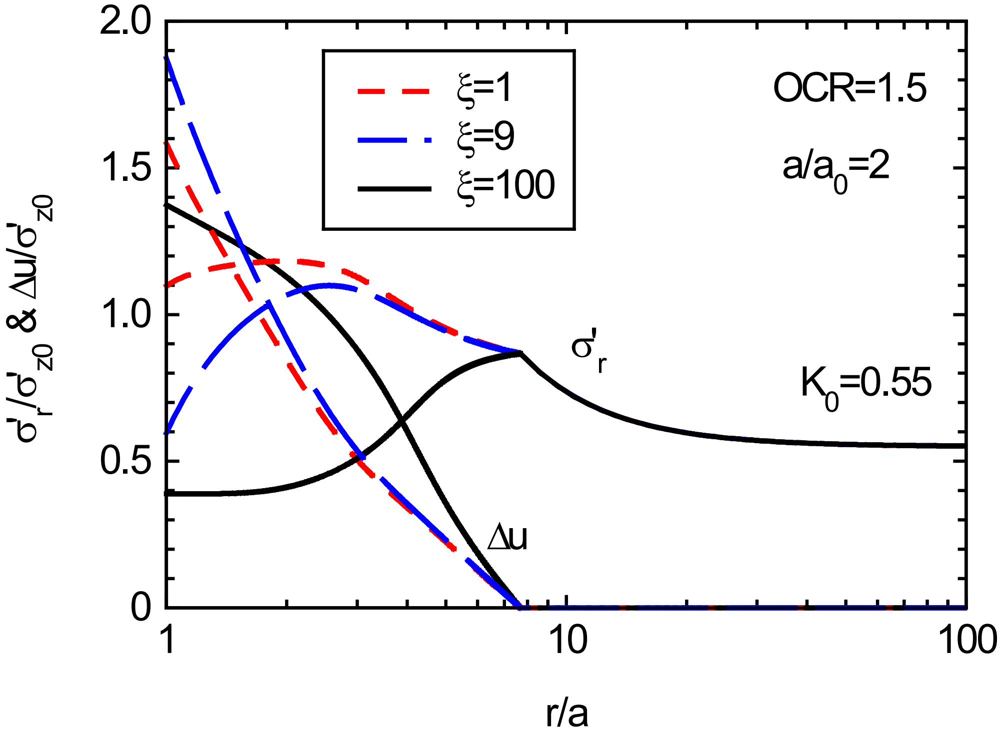

(b)

Figure 14. Stress distributions around the cavity: (a) Influence of radial displacement; (b) Influence of rate of debonding.

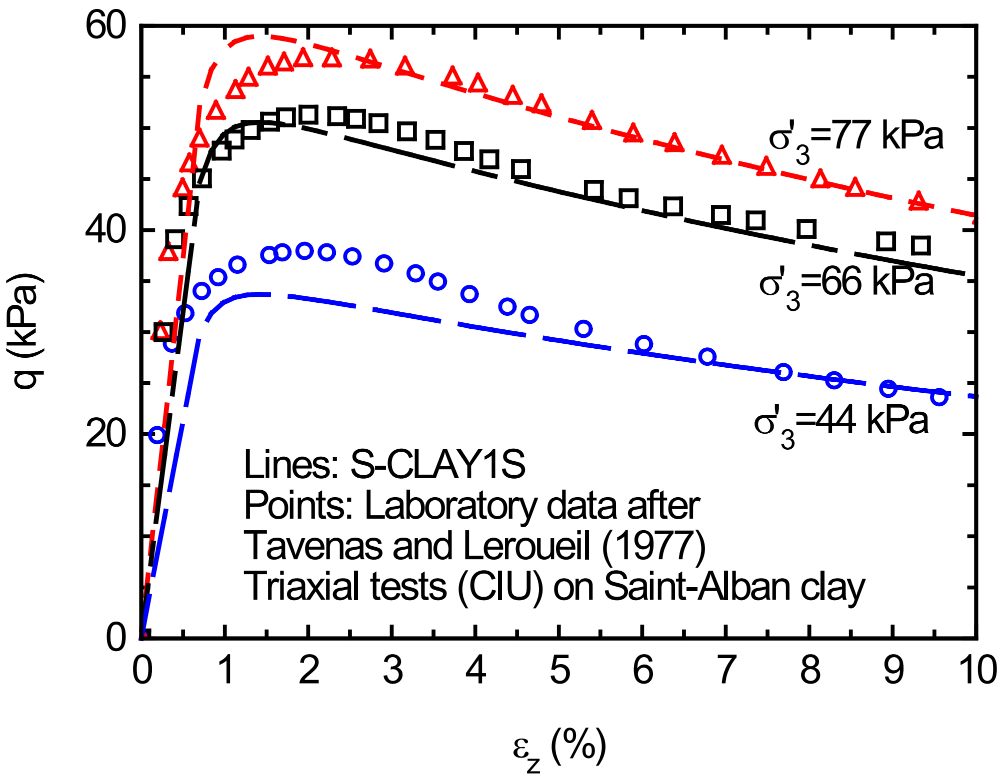

Figure 15. Calibration of Saint-Alban clay parameters for S-CLAY1S using triaxial tests.

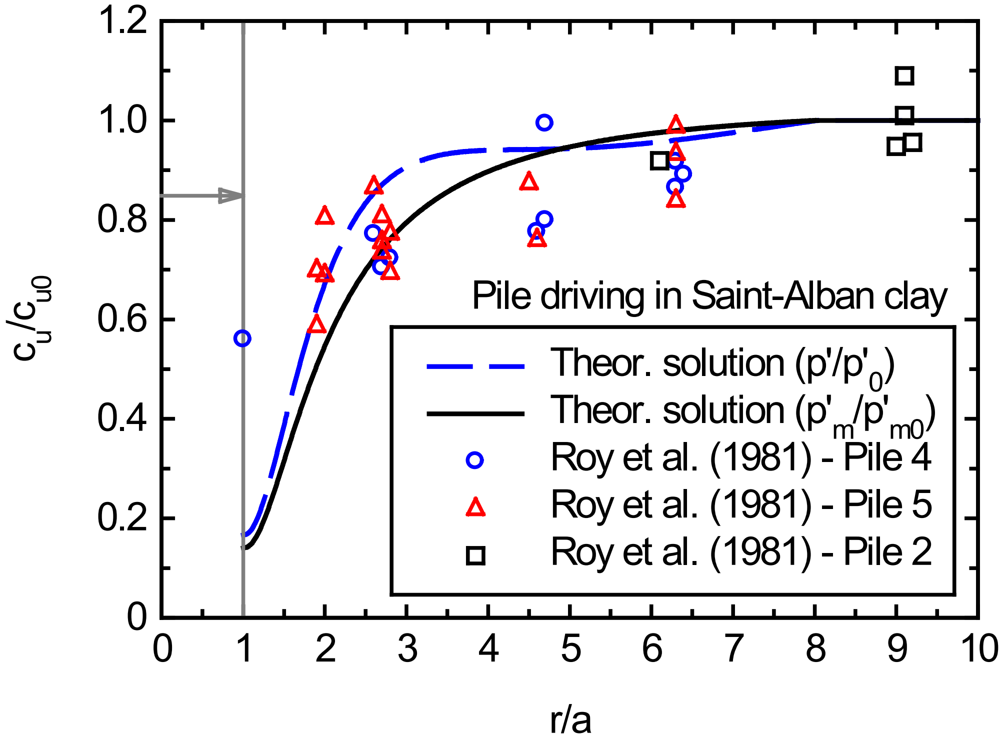

Figure 16. Variation of undrained shear strength immediately after pile driving in Saint-Alban clay. Comparison between field data and estimations using the theoretical solution.